IN-02

48393

P.73

NASA Contractor Report 4406

Viscous Computations of Cold Air/Air Flow Around Scramjet Nozzle Afterbody

Oktay Baysal and Walter C. Engelund

GRANT NAG1-811
OCTOBER 1991

NASA

NASA Contractor Report 4406

Viscous Computations of Cold Air/Air Flow Around Scramjet Nozzle Afterbody

Oktay Baysal and Walter C. Engelund
Old Dominion University
Mechanical Engineering and Mechanics Department
Norfolk, Virginia

Prepared for
Langley Research Center
under Grant NAG1-811

National Aeronautics and
Space Administration
Office of Management
Scientific and Technical
Information Program
1991

ABSTRACT

The design of the nozzle-afterbody section for a hypersonic transport such as the NASP is currently underway, and is being conducted using both computational fluid dynamics and cold, non-reacting, simulant gas experimental models. In this study, computations are performed for a cold gas simulation of a scramjet afterbody flowfield and compared with the results obtained from an experimental study of scramjet module nozzle-afterbody flows. The expansion of a supersonic flow through an internal/external nozzle–afterbody configuration and its viscous mixing with a hypersonic freestream flow of air is computed using two and three–dimensional upwind, finite volume, Navier-Stokes schemes. The Reynolds stresses are represented by a Baldwin-Lomax algebraic turbulence model with modifications to account for separated flow, multiple wall geometry, and turbulent wake flow. Two-dimensional computations for over-expanded (off design) and under-expanded nozzle flows, are performed on flow adapted grids, and three-dimensional results are obtained for a half-span nozzle model on a fixed grid. The results obtained from the adapted grid computations show improved accuracy and resolution. The computed pressure distributions compare favorably with experimental results. Furthermore, the results demonstrate that the solutions obtained from the computational fluid dynamics algorithms used in this study, can be used to expand the database for these types of nozzle-afterbody configurations.

TABLE OF CONTENTS

Page

LIST OF SYMBOLS

a = local speed of sound

C_p = coefficient of pressure

C_v = constant volume specific heat

e_t = total energy per unit volume

e = internal energy per unit volume

F, G, H = inviscid flux vectors

F_v, G_v, H_v = viscous flux vectors

J = transformation Jacobian

k = coefficient of thermal conductivity; also tension spring constant for adaptive grid algorithm

M = Mach number

n = normal distance from a boundary

p = pressure

Pr = Prandtl number

q = heat flux

Q = vector of conserved variables representing mass, momentum, and total energy per unit volume

R = universal gas constant

Re = Reynolds number

t = time

T = static temperature

u,v,w = cartesian velocities

U, V, W = contravariant velocities; V also denotes the volume of a computational cell

GREEK

δ = boundary layer thickness; also central difference operator

γ = ratio of specific heats

ξ, η, ζ = curvilinear coordinates

λ = bulk viscosity

τ = shear stress

ρ = density

ω= vorticity

μ = effective viscosity ($\mu_l + \mu_t$)

μ_l = molecular viscosity

μ_t = eddy (turbulent) viscosity

SUBSCRIPTS AND SUPERSCRIPTS

i, j, k = spatial indices

n = time level

w = wall condition

∞ = freestream conditions

Chapter 1

INTRODUCTION

General background information and motivation for this study are presented in this chapter. A brief survey of the related current literature, both experimental and computational, is provided along with the specific objectives of this study

1.1 Background

The recent resurgence of interest in hypersonic aerodynamics has come about largely in part due to the development of the National Aerospace Plane (NASP). The design of this type of aircraft will rely heavily on the use of computational fluid dynamics, since the operating conditions (Mach number, Reynolds number, enthalpy levels, etc.) prohibit the use of most of the conventional experimental facilities to obtain the required data for design analysis.

One of the major design tasks involved in the development of a hypersonic air-breathing aircraft is the integration of the engine and the airframe. This is necessary in order to reduce excessive drag and weight due to the high Mach numbers at which the aircraft will be traveling. Preliminary designs for an integrated propulsion system include a forebody/inlet system in which the forebody of the aircraft is used to partially compress the air before it enters the engine module. This is shown in the sketch of Fig. 1.1. The oncoming air is further compressed by a series of wedges and struts, and then mixed with a fuel and ignited in the combustor region. Finally, the high pressure combustion products are expanded through the combustor exit nozzle and over the airframe afterbody configuration. The overall propulsive efficiency of the nozzle is determined, to a large extent, by the exhaust plume flow over this afterbody section. This study is concerned primarily with this nozzle-afterbody region.

The design and testing of a scramjet nozzle-afterbody section using actual engine combustion products is impractical in a conventional wind tunnel. The actual chemistry and high total enthalpy levels of the exhaust products would be quite difficult to match in a scaled test section. However, several alternatives do exist. A simulant gas can be substituted for the actual combustion products, provided that dynamic and thermodynamic similitude are enforced. Perhaps a more economical alternative would be to do the preliminary design analysis using computational fluid dynamics (CFD). Since there is currently very little experimental data for very high Mach number flows, some means of calibrating and validating these CFD codes must be achieved before they can be used with complete confidence in this design process.

1.2 Computational and Experimental Literature on Nozzle-Afterbody Flows

In the 1970's, a study was undertaken by Grumman Aerospace Corporation under a NASA contract to develop an experimental cold gas simulation technique for scramjet exhaust flows [1–3]*. The purpose of this study was to define a method for accurately simulating pressure distributions on the nozzle-afterbody surfaces of a hypersonic scramjet aircraft using a cold substitute simulant gas, as opposed to the hot combustion product gases from the scramjet engine. It was determined in this study, that in addition to the usual nondimensional similitude parameter requirements for inviscid flows (i.e. Mach numbers, pressure ratios, temperature ratios, etc.), that the ratio of specific heats (γ) of the combustion products must also be matched by the simulant gases. This concept is discussed in further detail in Appendix A. It was also determined in this study that the surface pressures were relatively insensitive to small changes in the thermodynamic properties of the gases, but are very sensitive to flow perturbations caused by the nozzle geometry.

An extension of this work was carried out at the NASA Langley Research Center by Cubbage et al. [4–5] and Pittman [6]. Experimental data was obtained for a scaled scramjet nozzle-afterbody flowfield using both air and a Freon/Argon mixture as the simulant gas. Static pressures were measured on the afterbody surface, for both two-dimensional and three-dimensional flows, with various nozzle-afterbody geometries. The experimental data of [5] was compared with numerical data from two–dimensional Navier-Stokes and Euler algorithms. It was concluded

---

* The numbers in brackets indicate references

from the experimental results of [6] that the pressure drop in a supersonic expansion will be smaller for the Freon/Argon simulant gas than for air, and hence results in greater overall afterbody forces.

Novak and Cornelius [7] conducted subsonic and transonic experiments on a similar afterbody model using air as the simulant gas. Their work included three-dimensional laser velocimetry measurements for the subsonic test portion of the nozzle-afterbody flow field. Very little experimental data exists for off-surface flowfields of supersonic/hypersonic mixing flows. This data would be very important in calculating exhaust plumes and shear layers, which may cause interference on aerodynamic control surfaces of the aircraft.

Extensive numerical studies have been conducted on rocket and nozzle based flows without solid afterbody surface interaction, that is, the flow from a nozzle exit plane which flows directly into the freestream. Most of these studies focus mainly on the thrust and thrust vectors generated by the nozzle itself, and not on the actual afterbody flow field plume structures. However, there have been several of these types of studies which did attempt to analyze the downstream flow.

Deiwert [8] used the thin-shear-layer formulation of the Navier-Stokes equations in the study of supersonic axisymmetric flow over boattails containing a centered propulsive jet. Solutions were presented for jet flows expanding supersonically into a low pressure supersonic freestream flow, with an in-depth analysis of the afterbody flow structure. Comparison with experimental data showed good agreement in many of the key flow features such as exhaust plume shape and structure, and the location of the external compression shocks. However, the quantitative comparison of nozzle flow exit angle was poor, and thought to be due to the improper modeling of turbulent transport phenomena in the region of separated flow at the base of the nozzle.

Hoffman et al. [9] computed the afterbody flowfield of an axisymmetric rocket nozzle flowfield using a complete Navier-Stokes formulation algorithm. They presented the results of a grid refinement study which showed that the grid resolution is very important in regions of shear layers and recirculation. The computed results obtained on a "quality" grid, where the grid point spacing was very dense in regions where large gradients were expected to occur, compared much more favorably with the experimental results.

Goldberg et al. [10] studied afterbody flowfields at sonic and supersonic Mach numbers. They presented results obtained from an upwind Navier-Stokes solver using alternatively a k-ϵ or a Baldwin-Lomax turbulence model. Comparisons with experimentally obtained pressure data were very good, however both turbulence models were deemed inadequate near large regions of flow separation. They also found that finer grid clustering and more grid points were needed in order to resolve the intricate details of the flow

In recent years, with the renewed interest in hypersonics and propulsion airframe integration, there have been numerous computational studies related to nozzle-afterbody flows. Barber and Cox [11] presented an overview of computational works being conducted towards the design of hypersonic airbreathing aircraft, with a section specifically devoted to the integration of the propulsion system. Povinelli [12] provided a summary of the current computational works which are directly related to the propulsion systems, including the nozzle-afterbody section. Many of the works have concentrated on one particular aspect of the flow or its approximation, such as the turbulence modeling, adaptive gridding schemes, shear layer analysis, or real gas effects. Several of the studies which are directly related to this work are given here.

Ray et al. [13] presented two and three-dimensional results based on Euler (inviscid) calculations of single and multiple module scramjet afterbody flows using a Freon/Argon simulant gas mixture. Their results show good agreement with the experimental data of [3], however their calculations are based on the nozzle flow expansion into quiescent air, not the actual hypersonic flow of air. Also, since they are treating the flow as inviscid, shear layers and regions of separated flow can not be computed.

Hsu [14] conducted a study of adaptive gridding refinements based on various nozzle-afterbody configurations. Several cases were calculated with and without the use of adaptive grids, and the end result in most cases, especially those which contained free shear layers and strong shocks within the flow, was the fact that the use of flow adaptive grids is essential in improving solution accuracy.

Baysal et al. [15] performed a two-dimensional analysis of the experimental work carried out by Cubbage et al. [4–5] and Pittman [6]. In the work of [15] the flow was analyzed using two different algorithms. The first code used was an implicit, upwind, finite volume Navier-Stokes solver which assumed a constant specific-heat-ratio (γ). The second code was an explicit MacCormack based Navier-Stokes solver, which included coupled species continuity equations to account for variable γ due to the mixing of the simulant gas (Freon/Argon mixture) with the external freestream air. This work was extended by Baysal et al. [16, 17] to include three-dimensional flow and adaptive gridding methodology in the analysis. The two-dimensional computational meshes were refined using flow adaptive grids to enhance the computational solution in the regions of large gradients, and to reduce the overall computational error. Three-dimensional flow solutions were computed for the nozzle-afterbody test section and compared with the three-dimensional experimental surface pressure data of [5].

Harloff et al. [18] conducted two-dimensional Navier-Stokes analysis of scramjet nozzle flow fields at design and off–design conditions. In this study, both the nozzle exhaust flow and the external flow were assumed to be air. Nozzle afterbody flowfields were computed over a range of nozzle exit Mach numbers for over-expanded and under-expanded flows. Nozzle efficiencies were computed for all of the cases, however no experimental data was given for comparison with numerical results.

Edwards [19] studied the exhaust plume/afterbody interactions using the thin-layer Navier-Stokes assumption with a coupled species continuity equation. This allowed for the solution of a binary gas mixture flow. Computations were performed for the external flow of air (γ=1.4) mixing with a simulant gas (γ=1.26). Additional computations were done with the simulant gas assumed to be air (γ=1.4). It was concluded, from the computational results and a kinetic theory of gases rationalization, that the pressure drop in supersonic expansion will be smaller for the γ=1.26 gas than for the γ=1.4 gas, and hence produced greater afterbody forces.

Ruffin et al. [20] have used two-dimensional and three-dimensional upwind Navier-Stokes solvers to do a preliminary analysis of a planned nozzle-afterbody experiment. They conducted two-dimensional parametric studies over various Mach numbers, pressure ratios, and afterbody ramp angles to help determine the experimental model loads and optimum afterbody ramp angle and length. Three-dimensional calculations were performed to predict the shape of the jet plume and the flow spillage from the windward side of the model into the expanding flow region. The three-dimensional results were also to be used to determine optimal locations for experimental probes and flow measurement devices, and to aid in the design of side flow fences which are used to minimize the flow spillage.

1.3 Objectives

The main emphasis of this research effort is focused on developing a further understanding of scramjet nozzle-afterbody flowfields through the use of computational fluid dynamics. This study is being conducted in parallel with wind tunnel tests of scramjet nozzle-afterbody flowfields, so that the computational results obtained can be compared with experimental results in order to benchmark the solution algorithms.

The specific objectives of this study include:

(a) developing a means of computationally analyzing the two-dimensional viscous mixing of a scramjet exhaust flow with that of an external freestream flow.

(b) applying an adaptive gridding methodology to the results obtained in (a) to enhance the solution and reduce the computational error.

(c) extending the two-dimensional analysis to three-dimensions, with the intention of using the computational methods to augment the data base on scramjet nozzle-afterbody flows.

The basic physical characteristics of the scramjet nozzle-afterboby flowfields are discussed in Chap. 2. The governing equations and corresponding boundary conditions are given in Chap. 3, and the basic algorithm used in the solution of these equations, along with the grid generation methods are detailed in Chap. 4. Results and discussion are presented in Chap. 5, and some conclusions and recommendations are given in Chap. 6.

Chapter 2

PHYSICAL DESCRIPTION

Propulsion airframe integration is taking a vital role in the development of a hypersonic airbreathing aircraft such as the National Aerospace Plane. One of the underlying concepts of propulsion airframe integration is the incorporation of the external nozzle modules with the airframe controlling surfaces. In this study, the afterbody surface of the fuselage acts to expand the supersonic turbulent flow scramjet exhaust, hence becoming part of the nozzle. The expansion of exhaust products over the external nozzle–afterbody surface will produce large forces and pitching moments on the aircraft, therefore some means must be developed to accurately predict these values in the design and testing process.

The simulation of the nozzle exhaust using combustion products in a conventional wind tunnel is quite difficult, and is often performed with a substitute gas. Wind tunnel tests are being conducted at NASA Langley Research Center using several different simulant gases, including air and mixtures of Argon and Freon. It has been shown that the proper mixture of Argon and Freon can simulate the specific-heat-ratio (γ) of the hot scramjet exhaust products, in addition to matching the correct values of Mach numbers, pressure ratios, and temperature ratios [1–3] . This study is concerned with the computational analysis of the scramjet afterbody flowfield using air as the simulant gas (see Appendix A for a description of the simulant gas concept). This study was conducted in parallel with a computational analysis of the same scramjet nozzle-afterbody model using an Argon-Freon mixture as the simulant gas [15–17].

A wind tunnel model of a single module scramjet nozzle–afterbody configuration was constructed for testing in the NASA Langley 20–inch Mach 6 tunnel. The maximum Reynolds number of this tunnel is approximately 23×10^6/meter with stagnation pressure and temperature of 2.5 MPa and 480K, respectively. In Fig. 2.1, a two-dimensional cross sectional drawing of the model is shown. The simulant gas mixture is fed into a high pressure plenum chamber via a mounting strut. The gas in this plenum chamber is expanded through a converging-diverging supersonic nozzle to approximately Mach 1.7 at the combustor exit plane (location x_3 in the figure), where it is further expanded over the nozzle-afterbody section of the model. This supersonic exhaust flow also encounters a hypersonic (Mach 6) freestream air flow, through which mixing occurs in a free shear layer containing additional expansions and shock waves. Instrumented pressure taps are located along the external nozzle-afterbody surface to measure the static pressures over the ramp. In Fig. 2.2 an isometric drawing of the model is shown. A removable tapered flow fence is shown which, when in place, is used to simulate a quasi two-dimensional flow. When this fence is removed, the nozzle flow also mixes with the hypersonic freestream in the lateral direction through a spanwise expansion, causing the flow to become fully three-dimensional.

The design and analysis processes for this type of a nozzle-afterbody section is very complex due to the fact that many additional parameters must be considered, in addition to those which must be accounted for in conventional nozzles. This particular nozzle is highly asymmetric, and consists of an internal and an external portion. The forces and moments generated by most conventional nozzles can be determined by analyzing the flow up to the nozzle exit plane only. In this particular case, the analysis must extend further downstream due to the fact that the lower aft portion of the aircraft forms the external portion of the nozzle. The flow over this afterbody region will have a dramatic effect on the thrust vector and pitching moment generated by the engine module.

The location and structure of the shear layer also becomes a concern. The internal and external flow, which are initially separated by the nozzle cowl, join together and mix through a shear layer. In addition to the usual fluid and thermodynamic properties which vary across the shear layer, there is a large pressure gradient between the two flows, which causes the shear layer to bend inward or outward depending on the sign of the pressure gradient between the internal and freestream flows.

An additional flow phenomenon encountered in this study is flow separation. Flow separation occurs when the momentum of the flow within a boundary layer region becomes too small to overcome a positive (adverse) pressure gradient (i.e. $\frac{\partial p}{\partial \xi} > 0$). This results in the flow breaking away from the boundary, causing a backflow or reversed flow region. The actual point of two-dimensional separation can be loosely defined as the point where the velocity gradient near the surface in the direction normal to the boundary $(\frac{\partial u}{\partial n})_w$ becomes zero.

In the general case of supersonic nozzle flow, there are several exhaust conditions which may exist. Among these are overexpanded (off-design) flow at the nozzle exit plane, and underexpanded flow at the nozzle exit plane. These two exhaust conditions are discussed below. In the internal region of the nozzle, the upstream flow at the nozzle throat feeds downstream towards the afterbody surface and undergoes a centered expansion as it reaches the lower corner of the ramp. Another expansion occurs as the flow encounters the upper corner of the nozzle cowl. The wall boundary layers along the cowl surfaces become an expanding shear layer as the flow moves downstream past the nozzle exit plane.

In the case of overexpanded flow for the asymmetric nozzle of this study, as the flow reaches the nozzle exit plane, the static pressure is lower than that of the external freestream pressure, which results in a shock emanating from the tip of the nozzle cowl. A two-dimensional sketch of this type of flow is shown in Fig. 2.3. This type of flow would be highly undesirable in an actual flight condition since the shock wave impinges on the afterbody surface of the airframe. This could have an adverse effect on the stability and trim of the aircraft.

An underexpanded flow through the same asymmetric nozzle, results in the internal nozzle flow continuing to expand rapidly down the afterbody surface. In this case, the upstream internal nozzle flow goes through the same two centered expansions at the lower ramp corner and the upper cowl corner, but when the flow reaches the nozzle exit plane, instead of encountering a shock, it goes through the additional expansion to match the freestream conditions. At the tip of the cowl the interaction between the expanding jet and the external flow produces a lip shock and a contact discontinuity. The two-dimensional structure of this flow is shown in the sketch of Fig. 2.4.

If the internal nozzle flow is allowed to mix with the freestream flow laterally, the flow becomes three-dimensional, and the same type of shocks and expansions can occur in the spanwise direction. In this study, the two-dimensional overexpanded and underexpanded nozzle flows are examined computationally. The two-dimensional asymmetric nozzle is then extended in the lateral direction, from the sidewall reflection plate up to the spanwise plane of symmetry shown in Fig. 2.2. For this case, the flow structure is nearly the same as that of the two dimensional case (since the nozzle-afterbody region is spanwise symmetric), with the addition of a viscous boundary layer along the sidewall reflection plate. The flow in this case will remain essentially two-dimensional (i.e. there is no lateral expansion or compressions which would send expansion waves or shocks across the afterbody surface).

Chapter 3

FORMULATION AND GOVERNING EQUATIONS

The three-dimensional governing equations are given in detail in Sec. 3.1. The details of the Baldwin-Lomax turbulence model are discussed in Sec. 3.2, and the modifications to the model for this particular problem are given in Sec. 3.3..

3.1 Governing Equations

The equations used to describe the three-dimensional viscous flow of a compressible fluid are the time averaged Navier-Stokes equations. These equations in terms of mass averaged conserved variables can be written in vector cartesian coordinate form as:

$$\frac{\partial Q}{\partial t} + \frac{\partial (F - F_v)}{\partial x} + \frac{\partial (G - G_v)}{\partial y} + \frac{\partial (H - H_v)}{\partial z} = 0 \tag{3.1}$$

where

$$Q = \begin{Bmatrix} \rho \\ \rho u \\ \rho v \\ \rho w \\ e_t \end{Bmatrix} \tag{3.2a}$$

$$F = \begin{Bmatrix} \rho u \\ \rho u^2 + p \\ \rho u v \\ \rho u w \\ (e_t + p)u \end{Bmatrix} \quad , \quad F_v = \begin{Bmatrix} 0 \\ \tau_{xx} \\ \tau_{xy} \\ \tau_{xz} \\ \tau_{xx}u + \tau_{xy}v + \tau_{xz}w - \dot{q}_x \end{Bmatrix} \tag{3.2b}$$

$$G = \begin{Bmatrix} \rho v \\ \rho v u \\ \rho v^2 + p \\ \rho v w \\ (e_t + p)v \end{Bmatrix} \quad , \quad G_v = \begin{Bmatrix} 0 \\ \tau_{yx} \\ \tau_{yy} \\ \tau_{yz} \\ \tau_{yx}u + \tau_{yy}v + \tau_{yz}w - \dot{q}_y \end{Bmatrix} \tag{3.2c}$$

$$H = \begin{Bmatrix} \rho w \\ \rho w u \\ \rho w v \\ \rho w^2 + p \\ (e_t + p)w \end{Bmatrix} \quad , \qquad H_v = \begin{Bmatrix} 0 \\ \tau_{zx} \\ \tau_{zy} \\ \tau_{zz} \\ \tau_{zx}u + \tau_{zy}v + \tau_{zz}w - \dot{q}_z \end{Bmatrix} \tag{3.2d}$$

with the shear stress terms defined as

$$\tau_{ij} = \frac{M\infty}{Re}\left[\mu\left(\frac{\partial u_i}{\partial x_j} + \frac{\partial u_j}{\partial x_i}\right) + \lambda\frac{\partial u_k}{\partial x_k}\delta_{ij}\right] \tag{3.3}$$

where Stokes' hypothesis ($\lambda = -2/3\mu$) has been assumed. Heat flux terms are formed from Fourier's heat conduction law,

$$\dot{q}_i = -\left[\frac{\mu M_\infty}{Re\,Pr(\gamma - 1)}\right]\frac{\partial T}{\partial x_i} \tag{3.4}$$

The molecular viscousity, μ_l, is assumed to be a function of temperature only, and is computed using Sutherland's formula,

$$\mu_l = \mu_0\left(\frac{T}{T_0}\right)^{\frac{3}{2}}\frac{T_0 + S}{T + S} \tag{3.5}$$

where S is the Sutherland constant and μ_0 and T_0 are the reference viscosity and temperature, respectively. The effects of turbulence are modeled by adding an eddy viscosity, μ_t. This eddy viscosity is computed from an algebraic turbulence model and is discussed in detail in Sec. 3.2.

The total energy and internal energy are given by

$$e_t = e + \frac{1}{2}\rho\left(u^2 + v^2 + w^2\right) \qquad and \qquad e = C_vT \tag{3.6}$$

The equation of state used to close this system of equations is given by the simple ideal gas law,

$$p = (\gamma - 1)\rho e = \rho RT \tag{3.7}$$

For convenience, the governing equations are recast in non-dimensional form. The dependent variables have been non-dimensionalized as follows:

$$\rho^* = \frac{\rho}{\rho_\infty} \qquad x^* = \frac{x}{l} \qquad y^* = \frac{y}{l} \qquad z^* = \frac{z}{l} \qquad t^* = \frac{a_\infty t}{l}$$

$$u^* = \frac{u}{a_\infty} \qquad v^* = \frac{v}{a_\infty} \qquad p^* = \frac{p}{\rho a_\infty^2} \qquad e_t^* = \frac{e_t}{\rho_\infty a_\infty^2} \tag{3.8}$$

where the non-dimensionalized variables are denoted by an asterisk. The ∞ subscript indicates a freestream value, and l is a reference length. For convenience sake, the asterisks on the non-dimensionalized variables will be dropped henceforth.

These governing equations have been written in physical cartesian coordinates (x,y,z). They can however, be transformed to generalized curvilinear (body fitted) coordinate space (ξ,η,ζ). The curvilinear coordinates are related to the cartesian coordinates by:

$$\xi = \xi(x,y,z) \qquad \eta = \eta(x,y,z) \qquad \zeta = \zeta(x,y,z) \tag{3.9}$$

The transformed form of Eq. (2.1) can be written as

$$\frac{\partial \hat{Q}}{\partial t} + \frac{\partial\left(\hat{F} - \hat{F}_v\right)}{\partial \xi} + \frac{\partial\left(\hat{G} - \hat{G}_v\right)}{\partial \eta} + \frac{\partial\left(\hat{H} - \hat{H}_v\right)}{\partial \zeta} = 0 \tag{3.10}$$

with

$$\hat{Q} = Q/J \tag{3.11}$$

where J is the Jacobian of the coordinate transformation defined as

$$\begin{aligned} J &= \frac{\partial(\xi,\eta,\zeta)}{\partial(x,y,z)} \\ &= \left[x_\xi y_\eta z_\zeta + x_\zeta y_\xi z_\eta + x_\eta y_\zeta z_\xi - x_\xi y_\zeta z_\eta - x_\eta y_\xi z_\zeta - x_\zeta y_\eta z_\zeta\right] \end{aligned} \tag{3.12}$$

For further details on this transformation see Ref. 32. The inviscid and viscous flux vectors in the generalized curvilinear coordinate system are defined as

$$\hat{F} = \frac{1}{J}\left\{\begin{array}{c} \rho U \\ \rho U u + \xi_x p \\ \rho U v + \xi_y p \\ \rho U w + \xi_z p \\ (e+p)U \end{array}\right\} \quad , \quad \hat{F} = \frac{1}{J}\left\{\begin{array}{c} 0 \\ \xi_x \tau_{xx} + \xi_y \tau_{xy} + \xi_z \tau_{xz} \\ \xi_x \tau_{yx} + \xi_y \tau_{yy} + \xi_z \tau_{yz} \\ \xi_z \tau_{zx} + \xi_y \tau_{zy} + \xi_z \tau_{zz} \\ \xi_x b_x + \xi_y b_x + \xi_z b_x \end{array}\right\} \tag{3.13a}$$

$$\hat{G} = \frac{1}{J}\left\{\begin{array}{c} \rho V \\ \rho V u + \eta_x p \\ \rho V v + \eta_y p \\ \rho V w + \eta_z p \\ (e+p)V \end{array}\right\} \quad , \quad \hat{G} = \frac{1}{J}\left\{\begin{array}{c} 0 \\ \eta_x \tau_{xx} + \eta_y \tau_{xy} + \eta_z \tau_{xz} \\ \eta_x \tau_{yx} + \eta_y \tau_{yy} + \eta_z \tau_{yz} \\ \eta_x \tau_{zx} + \eta_y \tau_{zy} + \eta_z \tau_{zz} \\ \eta_x b_x + \eta_y b_x + \eta_z b_x \end{array}\right\} \tag{3.13b}$$

$$\hat{H} = \frac{1}{J}\left\{\begin{array}{c} \rho W \\ \rho W u + \zeta_x p \\ \rho W v + \zeta_y p \\ \rho W w + \zeta_z p \\ (e+p)W \end{array}\right\} \quad , \quad \hat{H} = \frac{1}{J}\left\{\begin{array}{c} 0 \\ \zeta_x \tau_{xx} + \zeta_y \tau_{xy} + \zeta_z \tau_{xz} \\ \zeta_x \tau_{yx} + \zeta_y \tau_{yy} + \zeta_z \tau_{yz} \\ \zeta_x \tau_{zx} + \zeta_y \tau_{zy} + \zeta_z \tau_{zz} \\ \zeta_x b_x + \zeta_y b_x + \zeta_z b_x \end{array}\right\} \tag{3.13c}$$

where U, V, and W are contravariant velocities defined as

$$\begin{aligned} U &= \xi_x u + \xi_y v + \xi_z w \\ V &= \eta_x u + \eta_y v + \eta_z z \\ W &= \zeta_x u + \zeta_y v + \zeta_z w \end{aligned} \tag{3.14}$$

and

$$b_i = u_j \tau_{ij} - \dot{q}_i \tag{3.15}$$

These equations can be greatly simplified for a two-dimensional flow by dropping the H and H_v vectors, and neglecting all derivatives in the ζ direction.

3.2 Turbulence Model

In order to properly model high Reynolds number flows, some method must be applied to predict the effects of turbulence within the fluid. The time averaged Navier-Stokes equations, given in Sec. 3.1, will only resolve the mean characteristics of the flow; they do not contain enough information to completely resolve the turbulent structure of the flow field. Therefore, a turbulence model is added to the set of governing equations to account for the effects of turbulence.

To this date, many different turbulence models have been formulated, none of which has been deemed universal to all types of flow. The biggest problem in modeling turbulence lies in the fact that many different length scales exist within a turbulent flow field. The two layer algebraic model of Baldwin and Lomax [21] is a widely accepted model due to its reasonable approximations of turbulent effects, and its ease of implementation in to a finite difference type of algorithm. Therefore, this is the model that has been chosen for this study. Several modifications have been made to this model to account for special conditions which exist in the flows of this study; these modifications are discussed in Sec. 3.3.

The Baldwin-Lomax model simulates the effects of turbulence by using an artificial eddy (turbulent) viscosity. The Reynolds stresses which arise from the time averaged Navier-Stokes equations are assumed to be proportional to the laminar stress tensor, where the coefficient of proportionality is defined as the eddy viscosity (μ_t). The Baldwin-Lomax model is a two layer model, and defines the eddy viscosity as:

$$\mu_t = \begin{cases} (\mu_t)_{inner} & , \quad y \leq y_{crossover} \\ (\mu_t)_{outer} & , \quad y > y_{crossover} \end{cases} \tag{3.16}$$

where y is the normal distance from the wall, and $y_{crossover}$ is the smallest value of y at which the values from the inner and outer formulas are equal.

In the inner region, the Prandtl-VanDriest mixing length formulation given as

$$(\mu_t)_{inner} = \rho\, l^2 |\omega| \tag{3.17}$$

where $|\omega|$ is the magnitude of the local vorticity vector, and

$$l=ky\left[1-exp\left(y^{+}/A^{+}\right)\right] \tag{3.18}$$

here,

$$y^{+} = \frac{y\sqrt{\rho_w \tau_w}}{\mu_w} \qquad (subscript\ w\ denotes\ wall\ values) \tag{3.19}$$

In the outer region

$$(\mu_t)_{outer} = \mathrm{K}\, C_{cp}\, \rho\, F_{wake}\, F_{kleb}(y) \tag{3.20}$$

with

$$F_{wake} = min\left\{ \begin{array}{c} y_{max}\, F_{max} \\ C_{wk}\, y_{max}\, u_{diff}^{2}\, / F_{max} \end{array} \right\} \tag{3.21}$$

where F_{max} is the maximum value of the function F(y) defined as:

$$F(y) = y|\omega|\left[1 - exp\left(-y^{+}/A^{+}\right)\right] \tag{3.22}$$

and y_{max} is the value of y at which F_{max} occurs. The function $F_{kleb}(y)$ is the Klebanoff intermittency factor, and is defined as:

$$F_{kleb}(y) = \left[1 + 5.5\left(\frac{C_{kleb}}{y_{max}}\right)^{6}\right]^{-1} \tag{3.23}$$

u_{diff} is the difference between the maximum and minimum total velocity at a fixed x (or ξ) station.

$$u_{diff} = \left(\sqrt{u^2 + v^2 + w^2}\right)_{max} - \left(\sqrt{u^2 + v^2 + w^2}\right)_{min} \tag{3.24}$$

The second term in u_{diff} is set to zero (except in wakes).

The constants which appear in Eqs. (2.21–27) are given the following values (from [21]):

$$A^{+} = 26$$

$$C_{cp} = 1.6$$

$$C_{kleb} = 0.3$$

$$k = 0.4$$

$$K = 0.0168$$

$$C_{wk} = 0.25$$

One major advantage of this model lies in the fact that the location of the boundary layer edge does not need to be computed, since the length scales are based on the distribution of vorticity.

3.3 Turbulence Model Modifications

The major difficulty encountered in applying the Baldwin-Lomax turbulence model to flows where regions of separation exist lies in the evaluation of a suitable length scale, y_{max}, and in turn determining $(\mu_t)_{outer}$ in the separated region. In Fig. 3.1a, a general F(y) curve is shown (Eq. (3.22)). If a region of separation or an overlying vortex exists, the F(y) curve may switch to that of Fig. 3.1b. In addition to the local peak in F(y) at y=a from the attached flow region, the separated flow region causes another peak to occur at y=b. The choice of this peak at y=b due to the separated flow results in an erroneous value of F_{wake} , and in turn, a value of $(\mu_t)_{outer}$ which is much too high. Thus, in general, the computed value of the eddy viscosity in the separated region will be too large, causing the details of the flow in this region to be washed out or distorted. In order to alleviate this problem, the Baldwin-Lomax turbulence model has been modified using the strategy of Degani and Schiff [22].

Degani and Schiff proposed cutting the F(y) curve off after the first peak is reached, so as not to pick the higher value of the second peak. In this method, the code searches for the first peak in F(y) outward from the wall to the free stream along each computational coordinate. A peak is considered to be found when the value of F(y) drops to 90% of the local maximum value. The value of 90% is somewhat arbitrary, and is chosen based on the type of flow being solved. In this case, the peaks in F(y) are spaced far enough apart such that the logic described will pick up the first peak. However, if additional separation occurs in the vicinity of the primary separation (e.g. crossflow separation in a three-dimensional flow), the second peak might be chosen, since F(y) does not drop to 90% of the local maximum after the first peak. This may be avoided by specifying a cutoff distance in terms of y_{max} from the previous local y_{max}, i.e. $y_{max} = Cy_{max(previous)}$, where C is a constant chosen equal to 1.5.

The second modification made to the standard Baldwin-Lomax model is the inclusion of multiple wall effects, for computing the value of μ_t near corners [23]. In this case, the eddy viscosity was computed as a singular function from each wall, and then an effective eddy viscosity was computed by taking an inverse average of the values computed from each wall. For example, on the corner bounded by the lower ramp surface and the viscous side wall, the eddy viscosity was computed as:

$$\mu_t = \frac{\left(\frac{\mu_t}{y^+}\right)_{lr} + \left(\frac{\mu_t}{y^+}\right)_{sw}}{\sqrt{(y^+)_{lr}^{-2} + (y^+)_{sw}^{-2}}} \tag{3.25}$$

Here the lr and sw subscripts denote lower ramp and side wall values respectively. The greater influence on the eddy viscosity is thus determined by the wall with the lower y^+ value.

The final modification made to the model is done so to account for the influence of the turbulence generated by the cowl which propagates into the shear layer. This is approximated by using a relaxation eddy viscosity model to represent the different length scales in the problem. Following the work of Waskiewicz, et. al., [24], the eddy viscosity in the wake is computed as:

$$\mu_t = (\mu_t)_c + [(\mu_t)_v + (\mu_t)_c][1 - exp(-x_c/\beta\delta_c)] \tag{3.26}$$

where $(\mu_t)_c$ is the calculated eddy viscosity at the tip of the cowl, and $(\mu_t)_v$ is the calculated "outer" eddy viscosity value based on the local vorticity value in the wake. The distance between these two stations is denoted by x_c, and δ_c is the instantaneous boundary layer thickness at the upper cowl tip. The parameter β is a relaxation length scale given a value of 10.

Chapter 4

SOLUTION ALGORITHM

The solution algorithms for both the two-dimensional and the three-dimensional governing equations are based on implicit finite-volume methods. In Sec. 4.1 the basic finite volume methodology is described. The time integration of the set of discretized equations is given in Sec. 4.2, and the implementation of the physical boundary conditions is discussed in Sec. 4.3. The computational grid generation methodology is discussed in Sec. 4.4.

4.1 Finite Volume Discretization

Both the two-dimensional and the three-dimensional sets of governing equations are solved using implicit finite volume schemes. In this method the integral formulation of the governing equations in conservation form is discretized directly in the physical space. This direct method of discretization ensures the conservation of mass, momentum, and energy at the discretized levels, even in the presence of strong discontinuities such as shocks. Equation (3.10) can be expressed in integral formulation as

$$\frac{\partial}{\partial t}\int\int\int_{v} \hat{Q} dV + \int\int_{s} \vec{F}\ \hat{n} dS = 0 \tag{4.1}$$

where the vector $\vec{F}$ is defined as

$$\vec{F} = \left(\hat{E} - \hat{E}_v\right)\hat{i} + \left(\hat{F} - \hat{F}_v\right)\hat{j} + \left(\hat{G} - \hat{G}_v\right)\hat{k} \tag{4.2}$$

and $\hat{n}$is a unit normal vector pointing outward from the surface S bounding the volume V,

$$\hat{n} = n_x\hat{i} + n_y\hat{j} + n_z\hat{k}. \tag{4.3}$$

The restriction of these equations to the two-dimensional equations is straightforward.

The flowfield is discretized into a set of ordered cells (volumes), and Eq. (4.1) is applied to each volume. The semi-discrete form of Eq. (4.1) at a cell whose location is i, j, k can be written as

$$\left(\frac{\partial \hat{Q}}{\partial t}\right)_{i,j,k} + \frac{\left(\hat{E} - \hat{E}_v\right)_{i+1/2,j,k} - \left(\hat{E} - \hat{E}_v\right)_{i-1/2,j,k}}{\Delta\xi}$$

$$+ \frac{\left(\hat{F} - \hat{F}_v\right)_{i,j+1/2,k} - \left(\hat{F} - \hat{F}_v\right)_{i,j-1/2,k}}{\Delta\eta}$$

$$+ \frac{\left(\hat{G} - \hat{G}_v\right)_{i,j,k+1/2} - \left(\hat{G} - \hat{G}_v\right)_{i,j,k-1/2}}{\Delta\zeta} = 0 \tag{4.4}$$

In the computational domain $\Delta\xi$, $\Delta\eta$, and $\Delta\zeta$ are arbitrary, and for convenience taken as

$$\Delta\xi = \xi_{i+1/2} - \xi_{i-1/2} = 1 \tag{4.5a}$$

$$\Delta\eta = \eta_{j+1/2} - \eta_{j-1/2} = 1 \tag{4.5b}$$

$$\Delta\zeta = \zeta_{k+1/2} - \zeta_{k-1/2} = 1 \tag{4.5c}$$

4.2 Time Integration of the Discretized Equations

The system of governing equations described in Sec. 4.1 is solved using an implicit, finite-volume, upwind, spatially factored scheme [25, 26]. This scheme employs upwind differencing for the convective and pressure terms, and central differencing for the diffusive terms. The upwind differences are constructed using a Roe flux-difference splitting method [27, 28].

Since the flows considered in this study are primarily steady-state in nature, a psuedo-time marching approach is used where the governing equations are treated as time dependent

Navier-Stokes equations. These equations are hyperbolic in time and allow for time marching or propagation type solutions.Equation (4.1) must first be linearized in time. The non-linear terms occur due to the fact that the flux vectors $\hat{E}$, $\hat{F}$, and $\hat{G}$ at the n+1 time level are functions of the vector of conserved variables $\hat{Q}$. This linearization is accomplished by expanding the flux vectors at (n+1) in a Taylor series about (n) as,

$$\hat{E}^{n+1} = \hat{E}^n + \left(\frac{\partial \hat{E}}{\partial \hat{Q}}\right)^n \left(\hat{Q}^{n+1} - \hat{Q}^n\right)\Delta t + \vartheta(\Delta t)^2 \tag{4.6a}$$

or

$$\Delta \hat{E}^n = A^n \Delta Q \Delta t + \vartheta(\Delta t)^2 \tag{4.6b}$$

where A is the flux Jacobian matrix $\frac{\partial \hat{E}}{\partial \hat{Q}}$. Similarly

$$\Delta \hat{F}^n = B^n \Delta \hat{Q}^n \Delta t + \vartheta(\Delta t)^2 \tag{4.7}$$

and

$$\Delta \hat{G}^n = C^n \Delta \hat{Q}^n \Delta t + \vartheta(\Delta t)^2 \tag{4.8}$$

where B and C are the flux Jacobian matricies $\frac{\partial \hat{F}}{\partial \hat{Q}}$and $\frac{\partial \hat{G}}{\partial \hat{Q}}$, respectively. The solution is marched in time by applying an implicit Euler integration scheme [26] to Eq. (4.4). Substituting Eqs. (4.6b), (4.7), and (4.8) into Eq. (4.4), and simplifying,

$$\left[\frac{I}{J\Delta t} + \frac{1}{\Delta\xi^i}\frac{\partial R}{\partial Q}\right]^n \Delta Q = -R(Q^n) \tag{4.9}$$

where $\Delta Q = Q^{n+1} - Q^n$, R^n is the steady-state residual evaluated at time level (n), and

$$R = \left[\frac{\partial\left(\hat{E} - \hat{E}_v\right)}{\partial \xi} + \frac{\partial\left(\hat{F} - \hat{F}_v\right)}{\partial \eta} + \frac{\partial\left(\hat{G} - \hat{G}_v\right)}{\partial \zeta}\right] \tag{4.10}$$

Substitution of Eqs. (4.6–8) into Eq. (4.9) yields:

$$\left[\frac{I}{J\,\Delta t} + \delta_\xi \frac{\partial\left(\hat{F} - \hat{F}_v\right)}{\partial Q} + \delta_\eta \frac{\partial\left(\hat{G} - \hat{G}_v\right)}{\partial Q} + \delta_\zeta \frac{\partial\left(\hat{H} - \hat{H}_v\right)}{\partial Q}\right] \Delta Q = -R^n(Q) \tag{4.11}$$

When Eq. (4.11) is written at discrete points in the computational domain, it results in a large banded matrix, which is expensive to solve computationally. One method of circumventing this problem is to use an approximately factored form of the equation. A number of different methods of factorization are possible for Eq. (4.11), one of which is the three-factor block-tridiagonal scheme [29] in which the implicit operator is split spatially such that each factored set contains flux Jacobians for its respective direction only. Applying this factorization to Eq. (4.11), one obtains

$$\begin{aligned}&\left[\frac{I}{J\,\Delta t}+\delta_\xi\frac{\partial\left(\hat F-\hat F_v\right)}{\partial Q}\right]\left[\frac{I}{J\,\Delta t}+\delta_\eta\frac{\partial\left(\hat G-\hat G_v\right)}{\partial Q}\right]\\&\left[\frac{I}{J\,\Delta t}+\delta_\zeta\frac{\partial\left(\hat H-\hat H_v\right)}{\partial Q}\right]\Delta Q^n=Res^n\end{aligned}\tag{4.12}$$

This method results in a set of block-tridiagonal matricies which can be solved in three computational sweeps. In the first sweep, the ξ–direction differences are treated as implicit,

$$\left[\frac{I}{J\Delta t}+\delta_\xi\frac{\partial\left(\hat F-\hat F_v\right)}{\partial Q}\right]\Delta Q^*=-R^n\tag{4.13}$$

where

$$\Delta Q^*=\left[\frac{I}{J\Delta t}+\delta_\eta\frac{\partial\left(\hat G-\hat G_v\right)}{\partial Q}\right]\left[\frac{I}{J\Delta t}+\delta_\zeta\frac{\partial\left(\hat H-\hat H\right)}{\partial Q}\right]\Delta Q^n\tag{4.14}$$

Equation (4.13) is solved for ΔQ^*. Equation (4.14) is then rearranged for the η–direction implicit sweep,

$$\left[\frac{I}{J\Delta t}+\delta_\eta\frac{\partial\left(\hat G-\hat G_v\right)}{\partial Q}\right]\Delta Q^{**}=\left(\frac{I}{J\Delta t}\right)\Delta Q^*\tag{4.15a}$$

where

$$\Delta Q^{**}=\left[\frac{I}{J\Delta t}+\delta_\zeta\frac{\partial\left(\hat H-\hat H_v\right)}{\partial Q}\right]\Delta Q^n\tag{4.15b}$$

Equation (4.15) is solved for ΔQ^{**}. Then Eq. (4.15b) is rearranged as follows, in order to solve for ΔQ^n,

$$\left[\frac{I}{J\Delta t} + \delta_\zeta \frac{\partial\left(\hat{G} - \hat{G}_v\right)}{\partial Q}\right] \Delta Q^n = \left(\frac{I}{J\Delta t}\right) \Delta Q^{**} \tag{4.16}$$

The vector of conserved variables is then updated to the next time level as:

$$Q^{n+1} = Q^n + \Delta Q^n \tag{4.17}$$

The upwind differences for Eqs. (4.13–16) are constructed using the flux-difference splitting method of Roe [26, 27]. In this method, the spatial derivatives are written conservatively as a balance across a volume element. For example in the ξ – direction the $\hat{F}$ flux difference at point i (holding the j and k indices constant) can be found as:

$$\left(\frac{\partial \hat{F}}{\partial \xi}\right)_i = \frac{\hat{F}_{i+1/2} - \hat{F}_{i-1/2}}{\Delta \xi} \tag{4.18}$$

where $\hat{F}_{i+1/2}$ and $\hat{F}_{i-1/2}$ are cell interface values, and can be constructed as:

$$\hat{F}_{i+1/2} = \frac{1}{2}\left[\hat{F}\left(Q^-_{i+1/2}\right) + \hat{F}\left(Q^+_{i+1/2}\right) - \left|\bar{A}\right|_{i+1/2}\left(Q^+_{i+1/2} - Q^-_{i+1/2}\right)\right]_{i+1/2} \tag{4.19a}$$

and

$$\left|\bar{A}\right|_{i+1/2} = \bar{T}_{i+1/2}\left|\bar{\Lambda}\right|_{i+1/2}\bar{T}^{-1}_{i+1/2} \tag{4.19b}$$

Here, A is the flux Jacobian matrix of $\hat{F}$, Λ is the matrix of eigenvalues of A, and T and T^{-1} are the right and left eigenvectors respectively. The overbars on the above variables denote Roe-averaged variables. Q^+ and Q^- denote conserved state variables on cell interfaces, which are obtained from the primitive variables as:

$$Q^-_{i+1/2} = Q_i + \frac{1}{4}\phi_\xi\left[\left(1 - \kappa_\xi\right) \nabla_\xi + \left(1 + \kappa_\xi\right)\Delta_\xi\right] Q_i \tag{4.20a}$$

$$Q^+_{i+1/2} = Q_{i+1} - \frac{1}{4}\phi_\xi\left[\left(1 + \kappa_\xi\right) \nabla_\xi + \left(1 - \kappa_\xi\right)\Delta_\xi\right] Q_{i+1} \tag{4.20b}$$

where

$$\Delta_\xi Q_i = Q_{i+1} - Q_i \qquad and \qquad \nabla_\xi Q_i = Q_i - Q_{i-1} \tag{4.21}$$

The order of differencing is determined by ϕ_ξ; for first order differencing ϕ_ξ is set zero, and for higher order differencing is set to one. The type of differencing is controlled by the parameter κ. $\kappa = -1$ corresponds to second order fully upwind differencing, $\kappa = 0$ corresponds to second order upwind biased, $\kappa = +1$ to second order central differencing, and $\kappa = 1/3$ to third order upwind biased.

In order to accelerate the convergence of the three-dimensional computations, two techniques, known as mesh sequencing and multigridding are employed [26]. A sequence of grids are formed over the computational domain by deleting every other grid line on the next finer grid. In mesh sequencing, the computations are started by iterating on the coarsest level grid, until the flow solution develops. Then, that solution is interpolated onto a finer level grid, where more iterations are performed, with an increased level of spatial resolution. This process is repeated until the finest level grid is reached (in this study, three levels are used). The rationale behind this mesh sequencing strategy lies in the fact that in the initial computations, when spatial resolution is not of vital importance, the calculations are performed on very coarse grids which helps to accelerate the development of the flowfield due to the large spatial steps.

Once the flow solution is developed on the finest level grid, the multigrid strategy begins. The multigridding technique uses the same coarser level grids which are created in the mesh sequencing progression, however instead of iterating on a coarser level and then moving up to the finer levels, the iterations are performed at the finest level first, and then cycled through to the coarser levels and back up again. There are several different cycling strategies which may be used, several of which are discussed in detail in [26]. The idea behind multigridding lies in the fact that the low frequency error components which occur on a given fine grid level can be reduced to high frequency errors by decreasing the grid resolution (i.e. using a coarser level grid). These high frequency errors on the coarser level grid are then reduced by applying the solution algorithm, which is much more capable of resolving high frequency errors. This process increases the overall robustness of the computational scheme, which allows for larger time steps to be used, and hence faster convergence rates.

4.3 Boundary Conditions

The initial and boundary conditions play an important role in the accuracy of the solution for a physical flow. Therefore, special attention must be paid to the formulation of these conditions.

The upstream boundary conditions for the nozzle and external regions are generated using the two-dimensional boundary layer profile program of [30]. In the internal nozzle region of the experimental model, the flow is expanded from a high pressure plenum through a convergent-divergent nozzle to a specified Mach number. However, there is no experimental data for the boundary layer thickness at this location (which corresponds to the upstream plane of the computational domain), so the computational boundary layer profiles for this location are generated in a somewhat arbitrary manner. The sum of the profile thicknesses from the lower ramp surface and the upper cowl surface inside the nozzle is assumed to be approximately 13 percent of the nozzle height. These boundary layer profiles are generated using the two-dimensional boundary layer program (assuming fully turbulent flow), and then mapped onto the computational grid's initial plane. The external flow profile is generated using the same two-dimensional boundary layer program by assuming a viscous turbulent flow over an 18" flat plate, which corresponds to the length of the upper cowl surface on the experimental model (Fig. 2.2). This results in a boundary layer thickness of approximately 0.5 inches. Were this code to be used as an actual design code for a nozzle-afterbody, it is likely that more detailed data would exist for the upstream profiles (either from more extensive experiments or from other computational results).

The upstream profiles for the three-dimensional calculations are generated using the same boundary layer profiles of the two-dimensional cases. These two-dimensional profiles are "stacked" along grid planes in the spanwise direction to form upstream profile planes. The presence of the third viscous sidewall (in both internal and external regions) causes a third boundary layer to develop, along with a very weak leading edge shock. In the actual corner flow regions, vorticies may exist; however in the present calculations these vorticies are not modeled. A somewhat more realistic method of simulating the upstream three-dimensional boundary layer profiles was used in [17] , although once again, as in the case of the two-dimensional calculations, there is no experimental data regarding the boundary layer thicknesses at these locations, so the profiles are somewhat arbitrary.

On regions bounded by solid surfaces, no-slip conditions are applied such that all velocities vanish at the boundary. These solid surfaces are also considered to be adiabatic. The pressure on a solid boundary is found from a zeroth-order-extrapolation from the interior point value. The density is then computed from the state equation.

$$u = v = w = 0 \quad , \quad \frac{\partial T}{\partial n} = 0 \quad , \quad \frac{\partial p}{\partial n} = 0 \tag{4.21}$$

The conditions at the outflow boundaries are set depending on the nature of the flow, be it subsonic or supersonic. If the flow is supersonic, all of the characteristic flow lines point from the inside of the computational domain outward, so that all of the variables at the outflow boundary may be determined from an extrapolation of the interior flow variables. If the flow is subsonic (e.g. within boundary layers) one of the characteristic lines is incoming (i.e. from outside of the computational domain inwards). Therefore, one of the boundary conditions must be specified analytically. In this case the freestream pressure is used. The remaining variables are extrapolated from the interior domain as before.

The boundary conditions on the plane of symmetry (three-dimensional case) are defined by extrapolation of all of the variables from the interior domain with the exception of the velocity component which lies perpendicular to the plane of symmetry. This normal component is set equal to the negative value of its interior point, thus forming a symmetry plane.

In this study, the two-dimensional computations are performed on a single body fitted grid. In order to allow for the application of the standard block tri-diagonal inversions from one end of the computational zone to the other in each direction (η=0 to $\eta_{\max}$ for η–implicit and ξ–sweep; ξ=0 to $\xi_{\max}$ for ξ–implicit and η sweep), some cells must coincide with the region bounded by the cowl. These cells are computed as if fluid were in this region, but they are then blanked out. This "blanking" is accomplished by (a) setting the off-diagonal blocks (which are 4x4 matrices) in the coefficient matrix to zero, (b) setting the diagonal elements of the diagonal blocks to unity, (c) setting the residual vector components to zero, (d) the Q values of the cells which neighbor fringe cells (cells which lie adjacent to "blanked cells") are set equal to the Q values of the fringe cells, in order to avoid incorrect flux computation at the cowl boundary. Thus, the specified wall boundary conditions for these cells are automatically preserved.

The three-dimensional computations are performed using a block structured approach. In this method, the physical space is divided into separate, distinct zones (in this case 4 zones have been used), where each block is treated as a separate computational domain. On blocks which lie next to each other, values of conserved variables are transferred across the interfaces along contingent cells. For example, the downstream boundary of one block becomes the upstream boundary of another. Conserved variables from two cells neighboring the boundary of one block are passed to the adjacent block as ghost cells, thus retaining the second order spatial accuracy of the scheme. The main drawback to this method lies in the fact that the lengths of the data vectors are restricted by the lengths of the blocks, which results in slower computational rates.

4.4 Grid Generation and Adaptive Grids

The physical domain over which the flow field is being sought needs to be discretized into a finite set of points, called the grid, to which the solution algorithms can be applied. Several methods exist for generating the computational grid, among them are algebraic methods, partial differential equation solvers (elliptic or hyperbolic), and complex variable transformation techniques. The proper choice of a grid is vital in generating accurate computational results for any flowfield. A grid which is not well suited to the flow can lead to instabilities in the computations or even a lack of convergence of the solution [33]. Grid density should be very high in regions where large gradients will exist (e.g. boundary layers, shocks, shear layers); however, the number of grid points used to discretize the flow field is limited by computer memory and speed, so a judicious choice of grid spacing is crucial. In this study, the domain is initially discretized using an algebraic grid generation scheme due to the ease of implementation and the fact that the physical boundaries of the flow domain are easily described by explicit algebraic functions. All of the clustering is based on an exponential stretching/clustering function given in [33]. In Fig. 4.1 the initial two-dimensional grid is shown. The grid point clustering on this grid is generated based on no a priori knowledge of the computational results. However, the basic flow physics described in Chap. 2 are assumed, and the clustering of grid points is seen to reflect this hypothesized flow. Along the ramp surface and around the cowl walls the grid is very dense in the normal direction in order to properly resolve the boundary layers. The grid is also clustered longitudinally near the corners on the ramp surface and on the inner cowl surface since it is expected that centered expansions will occur at these locations.

In addition to the computations on the fixed grid, flow adaptive grid calculations are performed for the two-dimensional cases. Once the solution develops on the fixed grid, the clustered and stretched regions of the grid are redefined based on the locations of large gradients in the flow. The method used to adapt the grid to these flow gradients is described in detail in Appendix B . The flowfield is then recomputed on the adapted grid.

The three-dimensional grid is generated using the same clustering strategy as that of the two-dimensional fixed grid, with additional clustering in the spanwise direction near the viscous reflection plate. As mentioned before, the three-dimensional solver utilizes the block structured approach, so actually, four grids are generated (one for each zone). The three-dimensional grid is shown from several perspectives in Fig. 4.2. A three-dimensional cutaway view of the entire grid is shown in Fig. 4.2a. The spanwise clustering can be seen on the upstream vertical plane. The inner nozzle region up to the cowl tip is shown in the enlarged view of Fig. 4.2b, and the spanwise symmetry plane, which is essentially the same as the two-dimensional grid, is shown in Fig. 4.2c.

The number of cells in each direction and the total number of cells of each grid are tabulated in Tabel 4.1. The description of each case (Case 1, 2, 3) are explained in the following chapter.

Chapter 5

RESULTS AND DISCUSSION

As mentioned previously, several different flow cases have been solved computationally. These cases will be referred to as:

Case 1: Two-Dimensional Overexpanded Flow (off-design)
Case 2: Two-Dimensional Nozzle Flow (design)
Case 3: Three-Dimensional Nozzle Flow (design)

The first case was initially intended as a trial run, to be used for code set up and initial validation of the grid. Although no experimental data exists for this case to compare the numerical solution, the results are being shown here due to the interesting nature of the flow. The second case was intended to be used as a benchmark of the two-dimensional code in that the computational results could be compared directly with the experimentally obtained results. The third case, which is simply an extension of the second case from two-dimensions to three dimensions, is also to be used in the validation process of the three-dimensional code set up. A summary of the upstream flow parameters for each case is given in Table 5.1.

Since the flows being solved are assumed to be steady state in nature, a local time stepping strategy is used. Each computational cell is advanced in time based on its maximum allowable Δt value. In order to stabilize the initial numerical transients, the time steps are gradually increased by increasing the Courant number from 0.01 to about 4.0. Table 5.2 shows the number of iterations and total CPU time required to obtain converged solutions. In the study, convergence is defined as the point where the logarithm of the residual (right-hand-side of Eq. (4.11)) is decreased by approximately four orders of magnitude.

The two-dimensional cases were run on the VPS-32 (an enhanced version of the Cyber 205) computer at NASA Langley Research Center. The three-dimensional runs were performed on the CRAY-2 computer, also located at NASA Langley Research Center, and used the mesh-sequencing/multigrid algorithm [26] described briefly in Chap. 4 to accelerate the convergence rate. It should be mentioned here that the computational rates achieved with these codes are very good in comparison with those required for a similar analysis using an explicit, finite difference, MacCormack scheme [15–17]. The multiple species analyses, which are reported in [15–17], are performed by assuming a mixture of four gases (Argon, Freon-13, Nitrogen, and Oxygen). This assumption leads to additional species continuity equations which are coupled to the global continuity, momentum, and energy equations. The two-dimensional, explicit, multispecies analysis code uses more than twice as much CPU time as does the implicit single gas analysis code used in this study. The additional CPU time required by the three-dimensional multispecies code is even more drastic. Almost ten times more CPU time on the CRAY-2 computer is needed to obtain converged solutions. The nozzle expansion rates for air are slightly higher than those for the multispecies stimulant gases, and thus the pressure distributions over the afterbody surface differs somewhat. However, for preliminary configuration analysis, the single gas, with constant specific-heat-ratio assumption seems to be a much more economical alternative to the multiple species studies.

In Figs. 5.1–2, the residual vs. iteration history is shown for Cases 1–2, respectively. In both Cases 1 and 2, the residual is reduced by approximately three orders of magnitude after about 7000 iterations on the fixed grid. Further iterations do not result in any additional decrease of the residual at this point. After 10,000 iterations, the grid is adapted to the flowfield, using the grid adaption scheme described in Appendix B. The error which results from the interpolation of the fixed grid solution onto the adapted grid causes the sharp increase in the residual values at this point. After an additional 6000 iterations, the residual is reduced by approximately four orders of magnitude, at which point it begins to level out again. Additional iterations at this point do not decrease the residual any further.

The residual history of Case 3 is shown in Fig. 5.3. The first 5000 iterations are performed on the coarsest level grid, at which point the residual is reduced by about one order of magnitude. The spikes which occur up to this point are the result of restarting the solution from a previous iteration level. This restarting strategy is required due to a CPU time constraint. After 5000 iterations on the coarsest level, the solution is "prolonged," or interpolated, onto the next finer level grid. An additional 1500 iterations are performed on this level, at which point the solution is "prolonged" to the finest level grid. The sharp increases in the residual values after 5000 and 6500 iterations occur due to the errors introduced by the interpolation from the coarser level grid to the finer level grids. The multigrid cycling strategy is invoked at this point, and the residual is seen to drop dramatically to the point where it is reduced by approximately four orders of magnitude.

5.1 Case 1

The results of this case 1, which depict the overexpanded nozzle flow, are presented in Figs. 5.4–8. This case was initially set up and run on the fixed grid (Fig. 4.1). The specific-heat-ratio (γ) was assumed to be constant and equal to 1.214, which corresponds to the specific-heat-ratio of the 72% Freon 28% Argon (by mass) mixture used as a simulant gas. The Mach number and static pressure contours obtained from solutions on the fixed grid are shown in Figs. 5.4 and 5.5, respectively. The internal nozzle flow goes through a centered expansion at the lower corner of the throat where the 20° afterbody ramp begins. This expansion fan strikes the lower cowl surface just upstream of the lower cowl corner where the flow undergoes a second centered expansion. At the point where the nozzle flow reaches the exit plane it is overexpanded with respect to the freestream external flow. This overexpansion results in a shock, with a pressure ratio of approximately 2.7, emanating from the tip of the cowl. This shock impinges on the afterbody surface about 1/3 of the distance down the length of the ramp, resulting in a weaker reflected shock. The shock-boundary layer interaction on the ramp also results in a separation bubble, or a region of reversed flow. The interaction between the internal and external flow occurs through an expansion and a shear layer, which also emanate from the cowl tip. The top expansion fan points upwards with an included angle of approximately 55°. The shear layer is pointed downward, following the same line as the afterbody surface, and eventually interacts with the reflected shock as it reaches the downstream portion of the ramp. The pressure ratio of the fully expanded downstream location to that of the upstream nozzle conditions is approximately 0.3.

The separation region on the ramp is further evidenced by the plot of velocity vectors with the streamlines superimposed (Fig. 5.6). In addition to the separation on the ramp caused by the shock-boundary layer interaction, a small region of reversed flow is observed right on the inside of the cowl tip. This is due to the rapid expansion of the external flow around the cowl tip, and the lower momentum of the boundary layer flow within the nozzle along the cowl wall.

Once the solution is obtained on the fixed grid, the adaptive gridding algorithm, described in Appendix B, is invoked. The grid is "adapted" to the specific flow field. Various parameters and combinations thereof may be used as weighting functions in the grid adaptation. In this case, a combination of the density (ρ) and the total velocity ($V=u^2+v^2$) is used. In regions where large gradients of ρ and/or V occur, the grid spacing will become very dense. This is shown in Fig. 5.7 where the adapted grid is seen to closely mimic the actual flow structure. The grid becomes very clustered where shocks and expansions occur, and somewhat sparse where there are no large gradients in velocity and density. One of the major problems encountered in applying the adaptive grid scheme to this particular flow geometry is the fact that the cowl boundaries protrude into the computational domain. If the adaption scheme was applied directly to the grid as a whole, the geometry of the cowl would be changed drastically, since very large gradients of density occur between the internal and external walls of the cowl. To alleviate this problem, the adaption process is split into two regions. In the first, the region from the upper cowl surface to the outflow boundary (y-direction) is adapted. The second region, which consists of all of the remaining area (i.e. everything that lies below the external boundary of the cowl surface) is then adapted. This method does place some restriction on the adaption of the lines dividing these two regions, however the flow gradients from the fixed grid solution do not appear to be excessively large here, so this is a minor inconvenience.

The Mach contours obtained from the solution on the adapted grid are shown in Fig. 5.8. The resolution of the solution near the shock regions is greatly enhanced over that obtained from the solution on the fixed grid, as can be seen by comparing Figs. 5.4 and 5.8.

5.2 Case 2

The results of this case 2, which depict the underexpanded nozzle flow, are shown in Figs. 5.9-15. This case was initially run using the same fixed grid as that of case 1, then rerun on the flow adapted grid generated using the fixed grid results. The same splitting strategy is used in this adaption, as was used in case 1, to avoid changing the geometry of the cowl. The final adapted grid is shown in Fig. 5.9. The calculations for this case were performed for air (γ=1.4) flowing supersonically in the nozzle region and hypersonically in the external region. These conditions match those of the experimental test case [6], so that the results can be compared directly with one another. In Fig. 5.10, the computational and experimental values of the ramp surface pressure coefficient (C_p) are compared. The experimental data is taken from the spanwise plane of symmetry, where the flow is essentially two-dimensional. The computed values are seen to agree quite well with the experimentally obtained values. The computational values of C_p are plotted on both the ramp surface and the inner cowl surface, and are seen to decrease abruptly at the corners, where the centered expansions occur, and gradually along the 20° ramp and 12° cowl. Additional experimental runs are currently being conducted at NASA Langley Research Center to generate off surface pressure data, so that the computational and experimental results can be compared in the shear layer region where the adaptive grid solution provides more resolution.

In Figs. 5.11 and 5.12, the density and the Mach number contours are shown from the fixed grid results. The nozzle flow goes through the same two centered expansions at the corners as the flow of case 1; however, when the flow reaches the exit plane it is underexpanded, and thus continues to expand down the ramp and outward into the freestream flow. In this case the shear layer, which originates at the cowl tip, is deflected upwards at an angle of 7°to 15°. This deflection of the inner region flow into the outer flow results in a weak external shock which turns the external flow upwards to match the flow direction of the shear layer. The improvement in the shear layer resolution obtained from using an adapted grid can be seen by comparing the Mach number contours from the fixed grid solution (Fig. 5.11) and those obtained from the flow adapted grid solution (Fig. 5.13). The velocity deficit extends much further downstream in the solution obtained on the adapted grid. This is also seen in the comparison of the velocity vectors plots of Figs. 5.14 and 5.15 (the fixed grid and adapted grid results, respectively). In this case, a slight region of reversed flow exists on top of the cowl, due to the rapidly expanding internal flow. This is easily seen in the velocity vector plot of the fixed grid results.

5.3 Case 3

The results of this case, which depict the three dimensional spanwise symmetric underexpanded nozzle flow, are shown in Figs. 5.16–19.In Fig. 5.16, nondimensional ramp surface pressures are shown at various spanwise locations. The computational pressures tend to agree with those obtained experimentally except upstream near the sharp expansion corner. This discrepancy may be due to the lack of sufficient grid clustering near the expansion region. The implicit damping which is inherent to upwind schemes tends to spread the expansion region out over several computational cells, which causes the computational pressures to lag the actual experimental values. The non-dimensional pressure contours, which are shown in Fig. 5.17 on the reflection plate and the afterbody ramp, indicate that the flow is essentially two-dimensional as would be expected. The flow structure is very similar to that of the flow in Case 2. The centered expansions occur at the lower ramp corner and the upper cowl corner in the same manner as before, and the flow continues to expand as it extends down the afterbody ramp and out into the freestream.

The nondimensional density contours for Case 3 are shown in Fig. 5.18. The view on the left shows the density contours on the spanwise plane of symmetry. A comparison with the density contours of Case 2 (Fig. 5.11) shows almost identical results. The centered expansions at the two corners inside the nozzle occur in the same fashion as in the flow of Case 2. The afterbody flow also continues to expand down the ramp and into the external freestream in the same manner as the two-dimensional flow, since it is not allowed (by the symmetry plane boundary conditions) to expand in the spanwise direction. The view on the right hand side of Fig. 5.18 shows the three-dimensional effects of the viscous sidewall. The density of the gas is higher near the viscous walls due to the increased temperature, which is a result of the adabatic wall boundary conditions which are imposed there.

The Mach number contours for case three are shown in Fig. 5.19. Again, the view on the left shows the Mach contours on the spanwise plane of symmetry. These contours are also very similar to those of the Mach contours obtained in the results of Case 2. The shear layer is approximately the same thickness, and is seen to be deflected outwards into the freestream region at nearly the same angle. However, the resolution inside the shear layer region is not as good as the results of Case 2, and is again thought to be the result of inadequate grid refinement. The view on the right shows a three–dimensional perspective view of the Mach contours. Here, the boundary layers and shear layers show up very well. Again, the flow is seen to be essentially two-dimensional in all respects, except near the viscous sidewall. The flow is seen to expand less rapidly near the sidewall, as evidenced by the downward dip in the Mach contours in the external flow region close to the wall. The wall boundary layer is essentially hindering the expansion into the freestream.

Chapter 6

CONCLUSIONS

The viscous mixing of a supersonic nozzle-afterbody flow with an external freestream flow is computed successfully for several cases. A two-dimensional overexpanded (off-design) nozzle flow is solved on both a fixed grid and a flow adapted grid. The results of the adapted grid solution show much better resolution of the recompression shock and the resultant shock boundary layer interaction region than those obtained on the fixed grid. The two-dimensional underexpanded nozzle-afterbody flowfield is also solved on a fixed and a flow adapted grid. In this case, the shear layer resolution is slightly better in the solution obtained on the flow adapted grid. The computational pressure distribution on the ramp surface compares favorably with the experimental surface pressures obtained at the nozzle symmetry plane.

The three-dimensional spanwise symmetric flow is solved on a multiblock, fixed grid. The results obtained compare well with the experimental surface pressure data and with the two-dimensional symmetry plane computations. This flow is essentially two-dimensional except near the regions bounded by the viscous reflection plate, and hence the flow structure is nearly the same as that of the two-dimensional case.

The Reynolds stresses are simulated using the Baldwin-Lomax two layer algebraic model with modifications to account for regions of separated flow, multiple wall geometries, and turbulent wake flow. There are many turbulence models available which may yield more accurate results. However, the simplicity of the Baldwin-Lomax model, and its ease of implementation into finite volume type codes, such as the ones used in this study, are the reasons for this choice. Any errors which may be due to the Baldwin-Lomax model should most likely show up in the shear layer region. There is no way to verify this, since there is currently no off-surface experimental data available. Also, since the occurrence and location of flow separation is strongly dependent on the nature of the flow, be it laminar or turbulent, the accuracy of the turbulence model used becomes very important if flow separation is a primary concern in the analysis.

Both the two-dimensional and the three-dimensional schemes used in this study are computationally very efficient methods for solving the complex flows about nozzle-afterbody sections. The use of an implicit based scheme, as opposed to an explicit MacCormack type algorithm, allows for larger time step increments to be used, and hence, faster convergence rates. The constant specific-heat ratio (γ) assumption for the internal simulant gas, leads to some deviation in the flowfield from that of an actual variable γ gas of scramjet exhaust products. But the savings in computational time achieved by using the constant γ assumption makes this an attractive alternative for use in the preliminary design stages of nozzle-afterbody configurations. The two-dimensional CFD capabilities which have been developed and demonstrated in this study should be used to augment the conventional wind tunnel studies of scramjet nozzle-afterbodies. However, in order to include the effects of spanwise expansions, three-dimensional calculations must be performed for the full-span nozzle.

Although the computational surface pressures agree well with those obtained experimentally, more measurements are needed to further validate these codes. A more accurate means of specifying the upstream boundary layer profiles is needed. This requires some experimental data on the boundary layer thicknesses at the nozzle throat. Also, off surface experimental flowfield data is needed, especially in the shear layer regions.

Additional three-dimensional computations are currently underway to include the spanwise expansion of the nozzle flow into the external freestream, along with computations using the Freon-Argon simulant gas mixture. Also, the use of three-dimensional flow adaptive grids should be studied, since the results from the two-dimensional adaptive computations show better resolution of the flow in high gradient regions.

REFERENCES

1. Oman, R. A., Foreman, K. M., Leng, J., and Hopkins, H. B.," Simulation of Hypersonic Scramjet Exhaust." NASA CR-2494, March 1975.
2. Hopkins, H. B., Konopka, W., Leng, J., "Validation of Scramjet Exhaust Simulation Technique." NASA CR-2688, June 1976.
3. Hopkins, H. B., Konopka, W., Leng, J., "Validation of Scramjet Exhaust Simulation Technique at Mach 6." NASA CR-3003, March, 1979.
4. Cubbage, J. M., Talcott, N. A. Jr., and Hunt, J. L., "Scramjet Exhaust Simulation Technique for Hypersonic Aircraft Nozzle Design and Aerodynamic Test," AIAA Paper 77–82, Jan. 1977.
5. Cubbage, J. M., Talcott, N. A. Jr., Hunt, J. L.,"Scramjet Exhaust Technique for Hypersonic Aircraft Design and Aerodynamic Tests," AIAA Paper 77–82, Jan. 1977.
6. Pittman, J. L., "A Mach 6 External Nozzle Experiment with Argon-Freon Exhaust Simulation," SAE Paper No. 892315, Aerospace Technology Conference and Exposition, Sept. 1989.
7. Novak, C. J. and Cornelius, K. C., "Investigations of Low-Speed Nozzle/Afterbody Performance for a Generic Hypersonic Configuration," AIAA Paper 88–0196, Jan. 1988.
8. 8. Deiwert, G. S., "A Computational Investigation of Supersonic Axisymmetric Flow Over Boattails Containing a Centered Propulsive Jet," AIAA Paper 83–0462, Jan. 1983.
9. Hoffman, J. J., Birch, S. F., Hopcroft, R. G., and Holcomb, J. E., "Navier-Stokes Calculations of Rocket Base Flows," AIAA Paper 87–0466, Jan. 1987.
10. Goldberg, U. C., Gorski, J. J., Chakravarthy, S. R., "Afterbody Flowfield Computations at Transonic and Supersonic Mach Numbers," AIAA Journal of Propulsion, Vol. 3, No. 1, Jan. 1987, pp. 56–62.
11. Barber, T. J. and Cox, G. B., "Hypersonic Vehicle Propulsion: A CFD Application Case Study," AIAA Paper 88–0475, Jan. 1988.
12. Povinelli, L. A., "Advanced Computational Techniques for Hypersonic Propulsion," NASA TM–102005, Sept. 1989.
13. Ray, R., Niggemeir, C., and Erdos, J., "CFD Analysis of 3–D Effects in Scramjet Exhaust Flow Fields," AIAA Paper 88–3262, July 1988.
14. Hsu, A. T., "The Effect of Adaptive Grid on Hypersonic Nozzle Flow Calculations," AIAA Paper 89–0006 Jan. 1989.
15. Baysal, O., Engelund, W. C., and Tatum, K. E., "Navier-Stokes Calculations of Scramjet-Afterbody Flowfields," ASME Symposium on Advances and Applications in Computational Fluid Dynamics, FED–Vol. 66 (Ed. O. Baysal), Nov. 1988, pp. 49–59.

16. Baysal, O., Engelund, W. C., Eleshaky, M. E., and Pittman, J. L., "Adaptive Computations of Multispecies Mixing Between Scramjet Nozzle Flows and Hypersonic Freestream," AIAA Paper 89–0009, Jan. 1989.

17. Baysal, O., Eleshaky, M. E., Engelund, W. C., "2–D and 3–D Mixing Flow Analysis of a Scramjet-Afterbody Configuration," Paper No. 14, International Conference on Hypersonic Aerodynamics, The Royal Aeronautical Society, Sept. 1989.

18. Harloff, G. J., Lai, H. T., and Nelson, E. S., "Two-Dimensional Viscous Flow Computations of Hypersonic Scramjet Nozzle Flowfields at Design and Off-Design Conditions," AIAA Paper 88–3280, July 1988.

19. Edwards, T., "The Effect of Exhaust Plume/Afterbody Interaction On Installed Scramjet Performance," AIAA Paper 89–0032 Jan. 1989.

20. Ruffin, S. M., Venkatapathy, E., Keener, E. R., Nagaraj, N., "Computational Design Aspects of a NASP Nozzle/Afterbody Experiment," AIAA Paper 89–0446, Jan. 1989.

21. Baldwin, B. S., and Lomax, H., "Thin Layer Approximation and Algebraic Model for Separated Turbulent Flows," AIAA Paper 78–257, Jan. 1978.

22. Degani, D., and Schiff, L. B., "Computation of Turbulent Supersonic Flows Around Pointed Bodies Having Crossflow Separation," Journal of Computational Physics, Vol. 66, No. 1, Sept. 1986, pp. 173–196.

23. Baysal, O., Srinivasan, S., "Calculation of Wall and Free Turbulent-Shear Flows at Supersonic Speeds, "ASME-FED, Vol. 51, Forum on Turbulent Flow (Ed. W. Bower) June 1987, pp. 55–60.

24. Waskiewicz, J. D., Shang, J. S., and Hankey, W. L., "Numerical Simulation of Near Wakes Utilizing a Relaxation Turbulence Model, " AIAA Journal, Vol. 18, No. 12, Dec. 1979, pp. 1440–1445.

25. Rumsey, C. L., Anderson, W. K., "Some Numerical and Physical Aspects of Unsteady Navier-Stokes Computations Over Airfoils Using Dynamic Meshes," AIAA Paper 88–0329, Jan. 1988.

26. Anderson, W. K., Thomas, J. L., and Whitfield, D. L., "Three-Dimensional Multigrid Algorithms for the Flux-Split Euler Equations," NASA TP-2829, Nov. 1988, pp. 4–13.

27. Roe, P. L., "Characteristic-Based Schemes for the Euler Equations," Annual Review of Fluid Mechanics, Vol. 18, 1986, pp. 337–365.

28. Roe, P. L., "Approximate Reimann Solvers, Parameter Vectors, and Difference Schemes," Journal of Computational Physics, Vol. 43, 1981, pp. 357–372.

29. Beam, R. M. and Warming, R. F., "An Implicit Finite-Difference Algorithm for Hyperbolic System in Conservation-Law Form," Journal of Computational Physics, Vol. 22, No. 1, Sept. 1976, pp. 87–110.

30. Julius, E. H. and Blanchard, D. K., "Computer Program for Solving Laminar, Transitional, or Turbulent Compressible Boundary Layer Equations for Two-Dimensional and Axisymmetric Flow," NASA-TM-83207, 1982.

31. Nakahashi, K., and Deiwert, G. S., "A Practical Adaptive-Grid Method for Complex Fluid-Flow Problems," NASA TM-85989, 1985.

32. Nakahashi, K., and Deiwert, G. S., "A Self-Adaptive Grid Method with Application to Airfoil Flows," AIAA Paper 85–1525, Jan. 1985.

33. Anderson, D. A., Tannehill, J. C., and Pletcher, R. H., Computational Fluid Dynamics and Heat Transfer, pp. 519–525, McGraw-Hill Book Company, New York, 1984, pp. 519–525.

Table 4.1 Computational grid sizes

Case	Block	idim	jdim	kdim	Total
1	1	155	1	132	20,305
2	1	155	1	132	20,305
3	1	33	25	41	217,300
3	2	49	25	41	
3	3	65	25	41	
3	4	65	25	41	

Table 5.1 List of upstream conditions for three cases

Case No.	Mach No. (int/ext)	Re/m (int/ext)	T_t (K) (int/ext	p_t (kPa) (int/ext)	γ
1	1.7	4.92×10^5	467	172	1.214
	1.7	4.92×10^5	467	172	
2	1.665	1.26×10^7	475	1166	1.4
	6.0	2.27×10^7	478	2520	
	6.0	2.27×10^7	475	1166	1.4
			478	2520	

Table 5.2 CPU time requirements for each case

Case	Iterations to convergence	Total CPU time	Speed (time/iteration/gridpoint)	Computer
1	4500*	6,000 sec	34 μsec	VPS-32
2	4500*	6,000 sec	34 μsec	VPS-32
3	7300*	8,400 sec	76 μsec	CRAY-2

*including grid adaption

**with mesh sequencing and multigriding

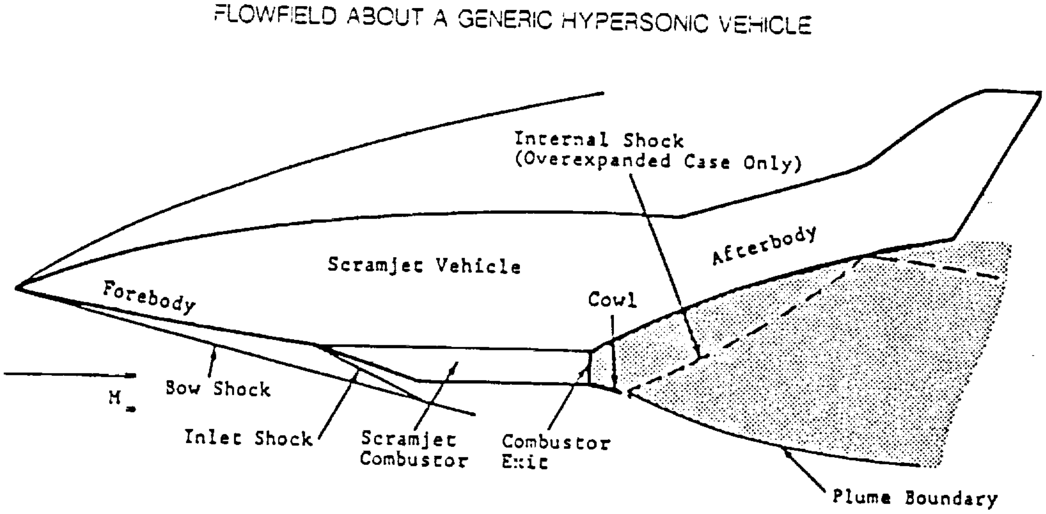

Fig. 1.1 Generic Hypersonic Aircraft

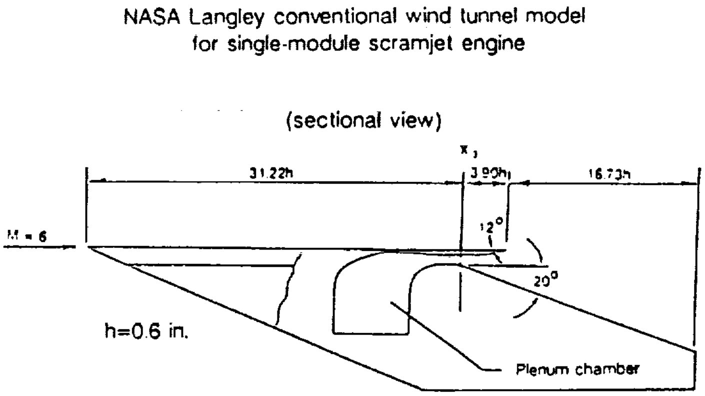

Fig. 2.1 Two-dimensional sectional view of the model

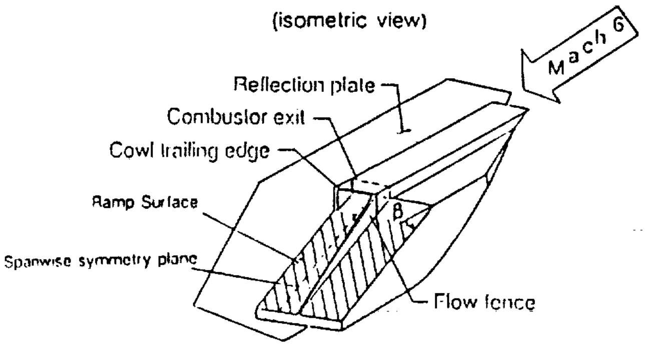

Fig. 2.2 Three-dimensional isometric view of the model

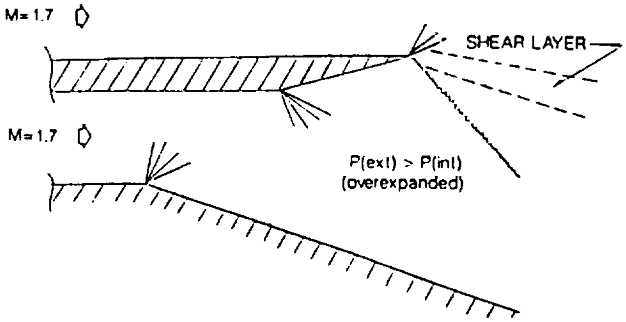

Fig. 2.3 Sketch of the overexpanded nozzle flow

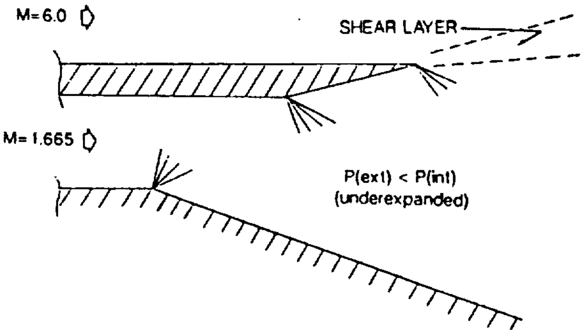

Fig. 2.4 Sketch of the underexpanded nozzle flow

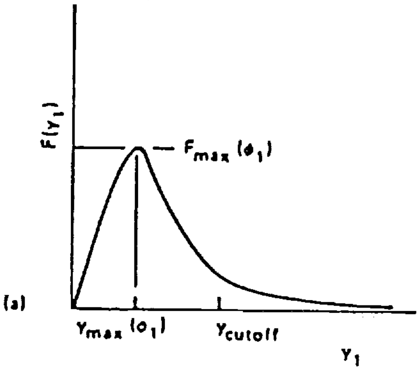

Figure 3.1a Behavior of F(y) in a attached boundary layer

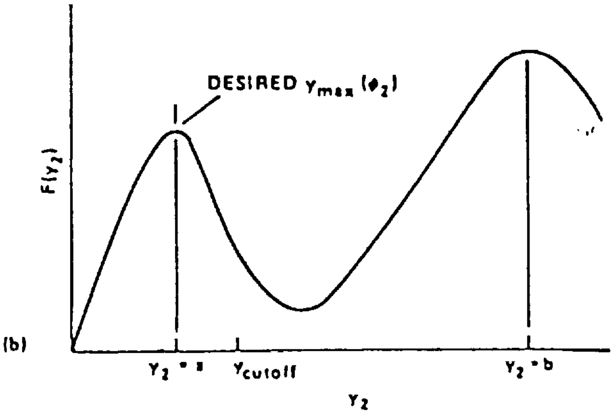

Figure 3.1b Behavior of F(y) in a separated boundary layer

Fig. 3.1 Behavior of F(y)

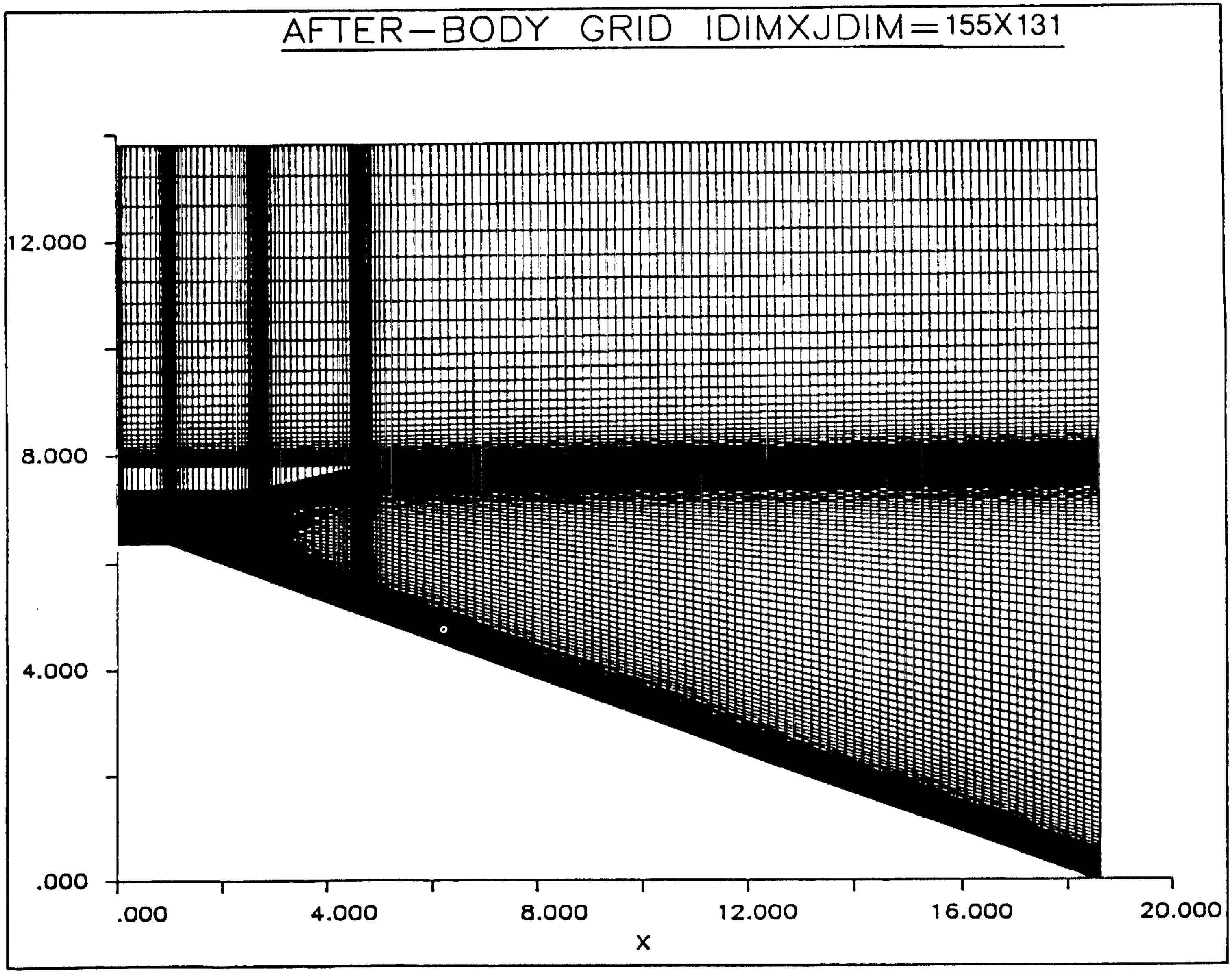

Figure 4.1 Two-dimensional fixed grid

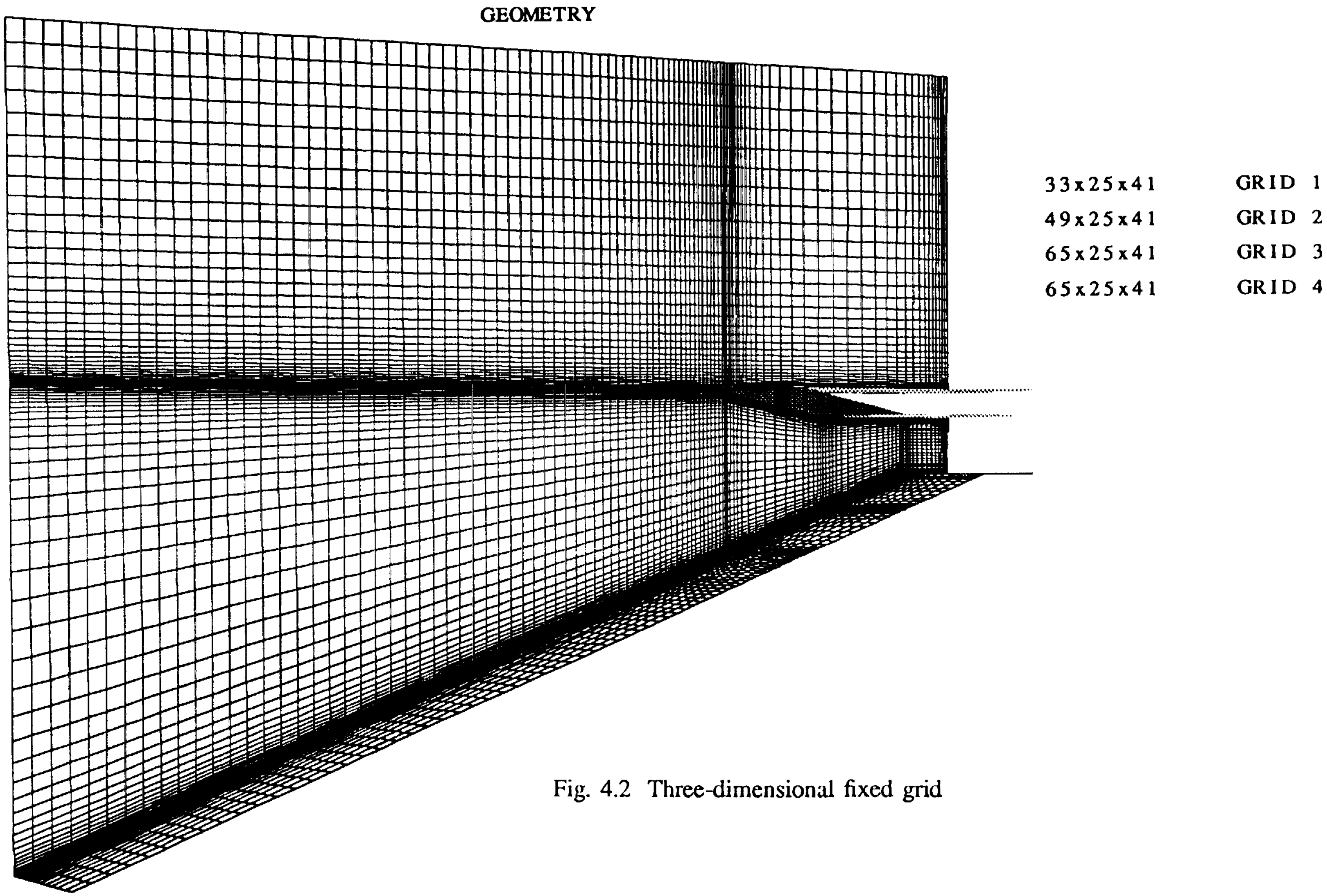

Fig. 4.2 Three-dimensional fixed grid

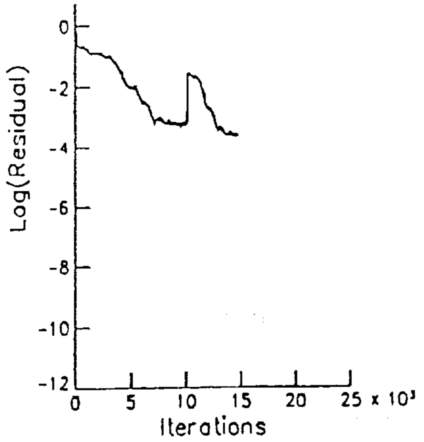

Fig. 5.1 Case 1 Residual vs. Iteration

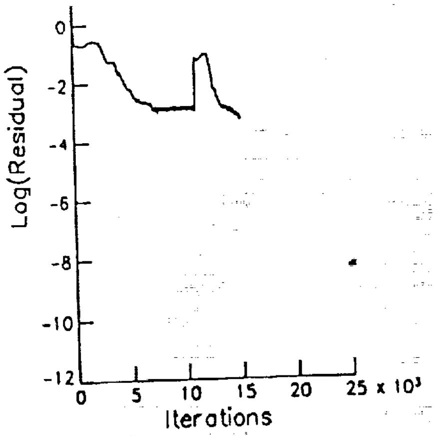

Fig. 5.2 Case 2 Residual vs. Iteration

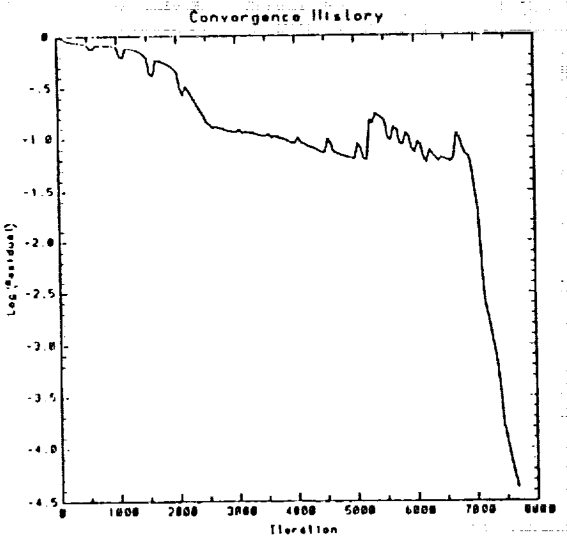

Fig. 5.3 Case 3 Residual vs. Iteration

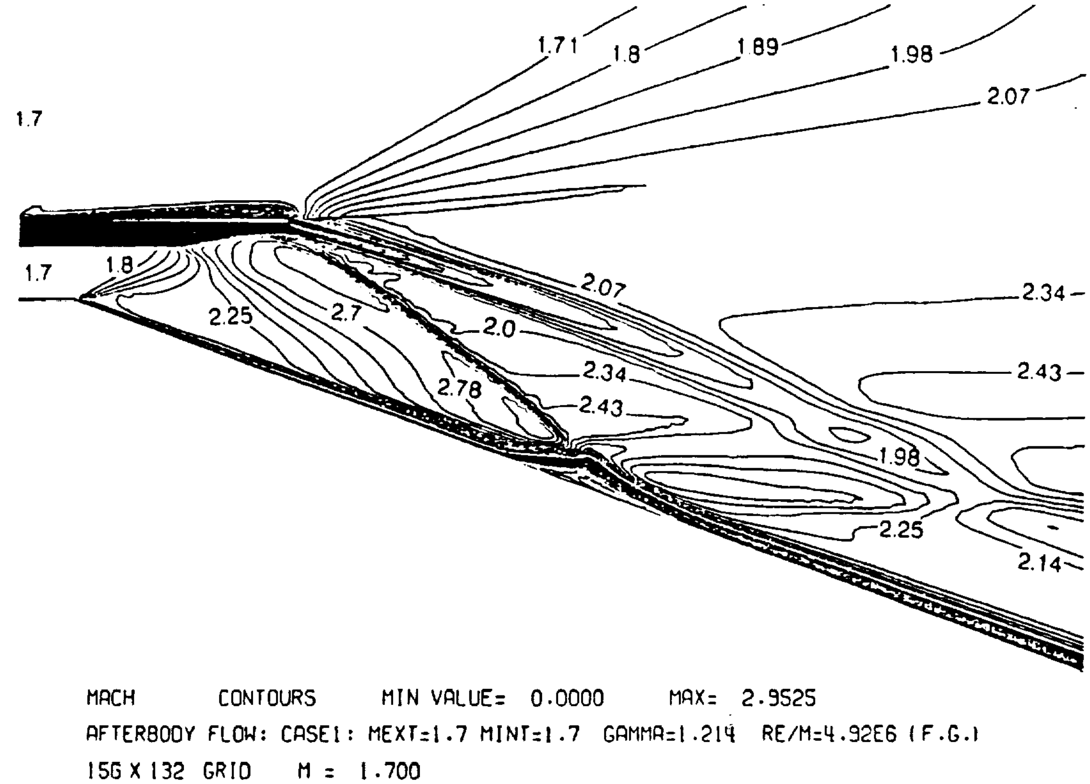

Figure 5.4 Case 1 Mach contours (fixed grid)

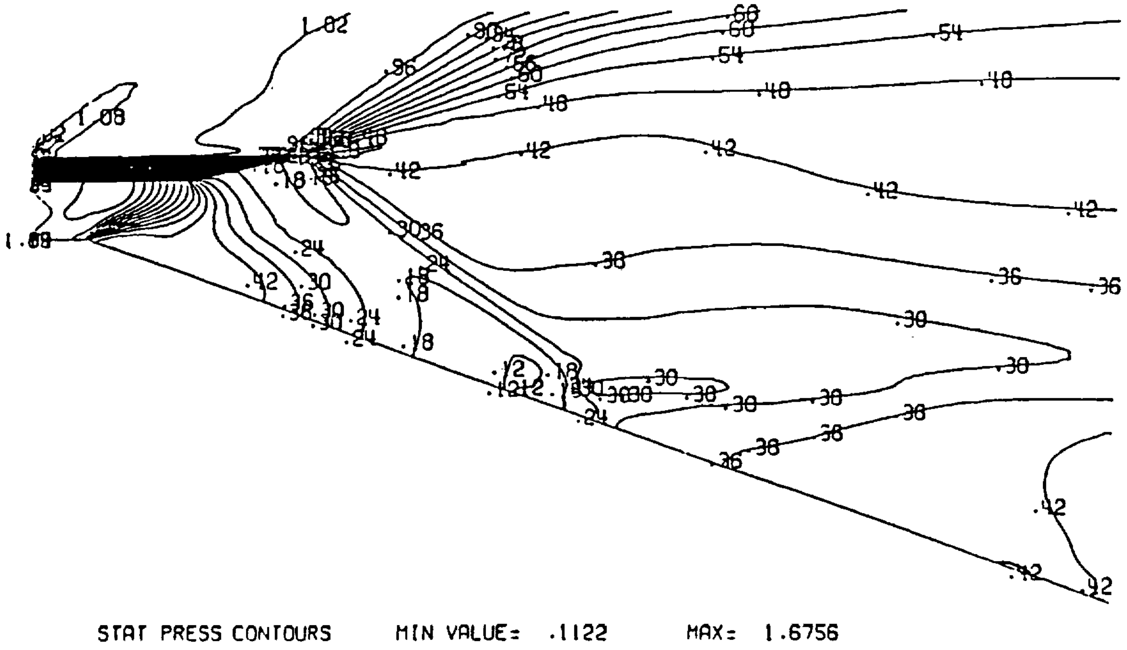

Figure 5.5 Case 1 static pressure contours (fixed grid)

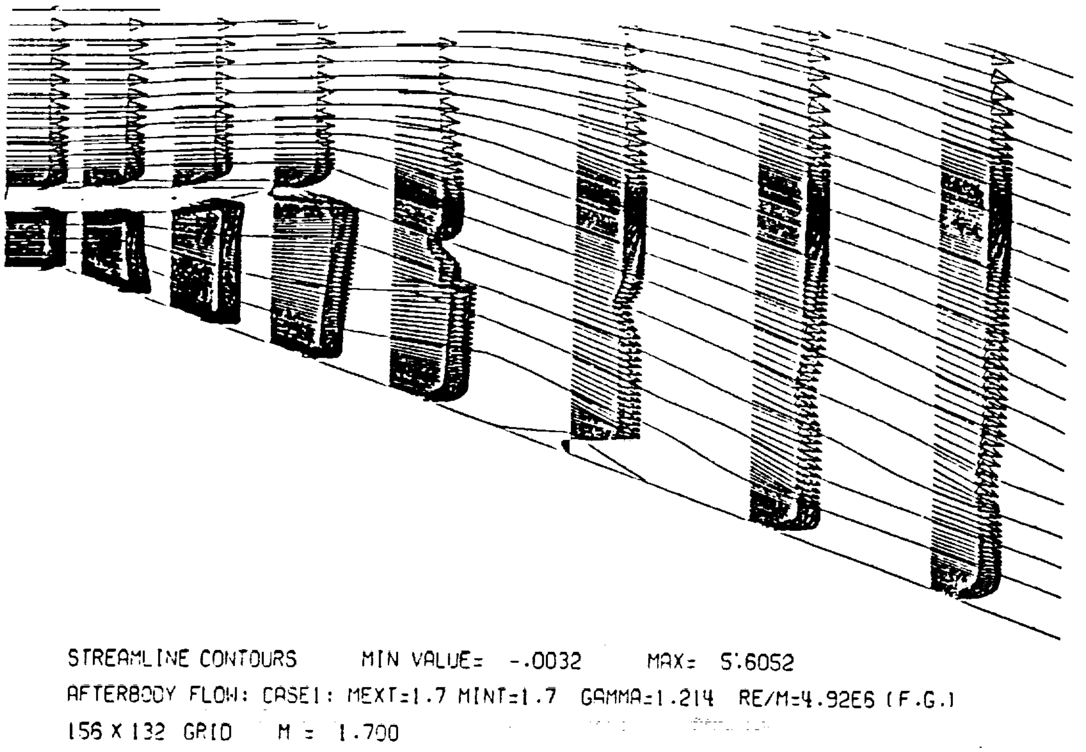

Figure 5.6 Case 1 streamline/velocity vectors (fixed grid)

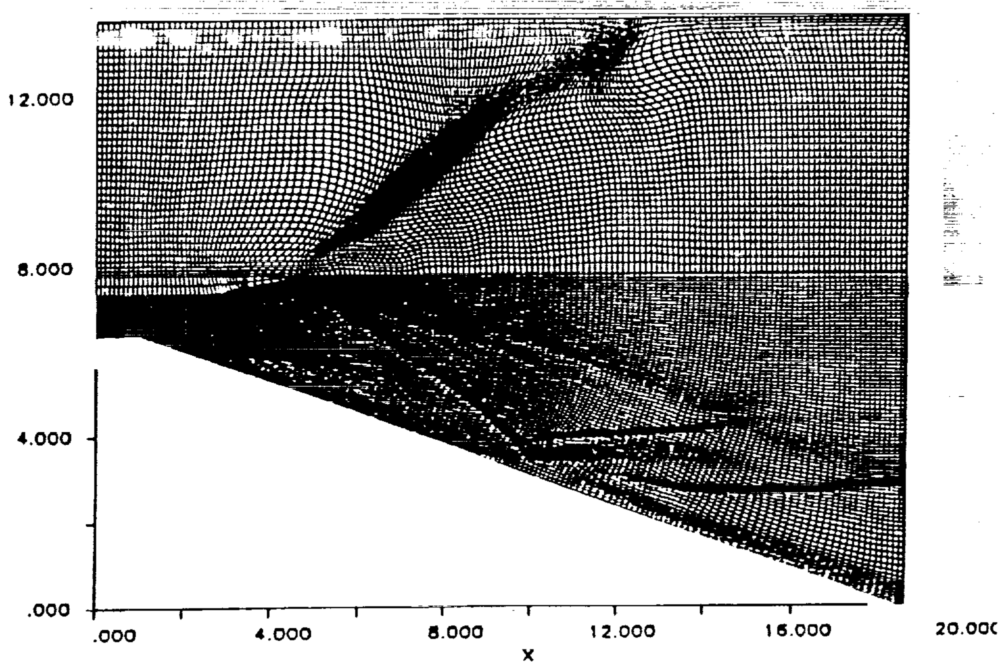

Figure 5.7 Case 1 adapted grid

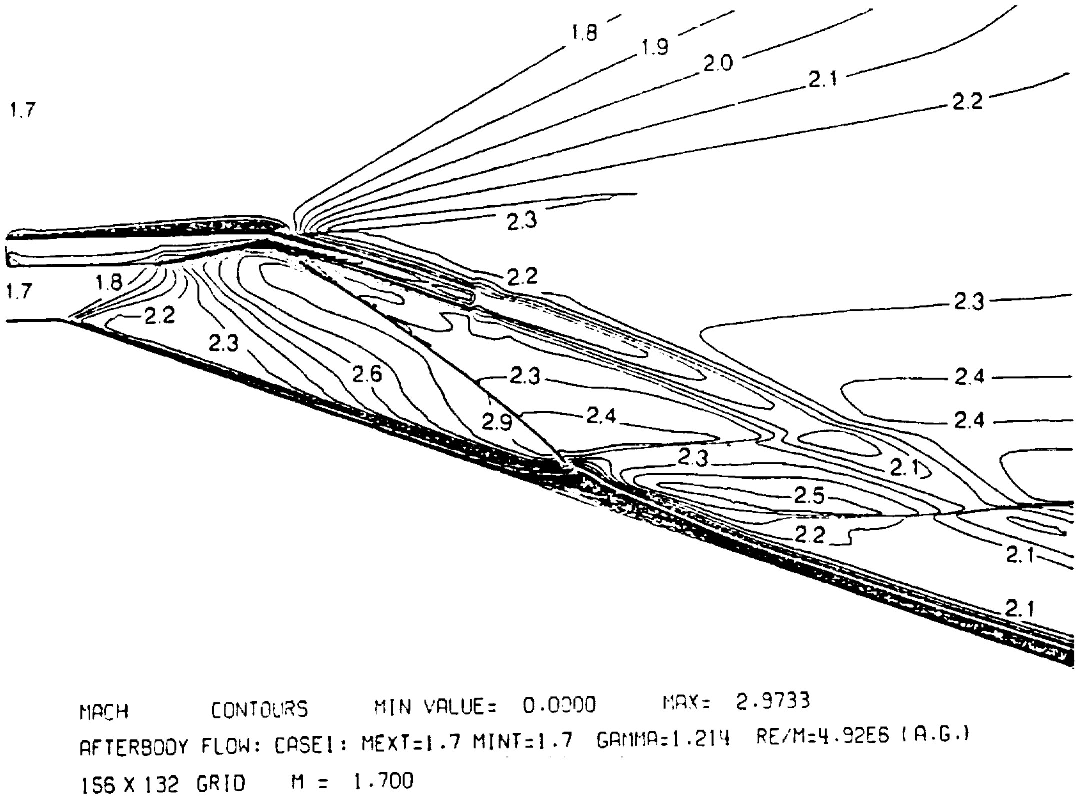

Figure 5.8 Case 1 Mach contours (adapted grid)

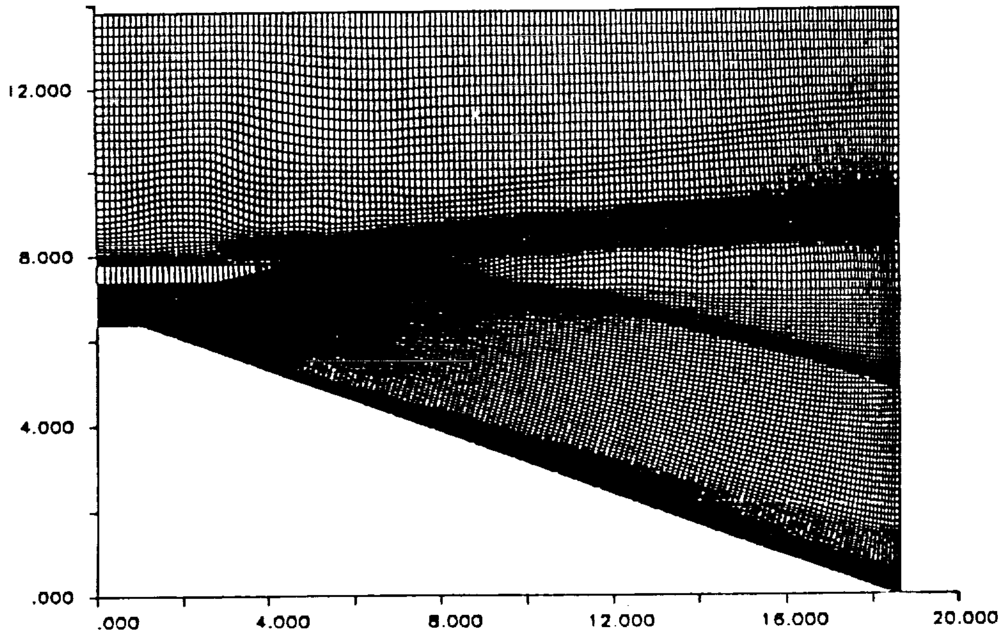

Figure 5.9 Case 2 adapted grid

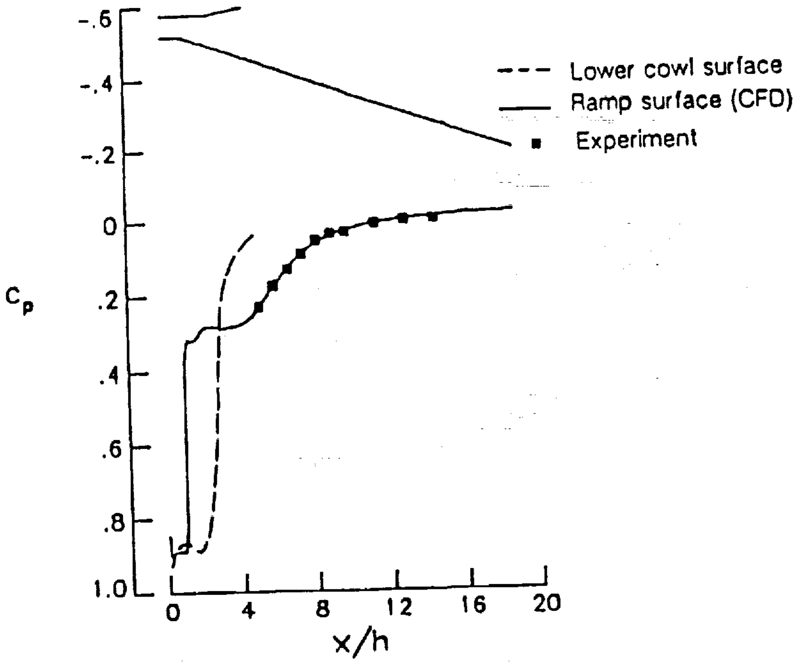

Figure 5.10 Case 2 surface pressure coefficient

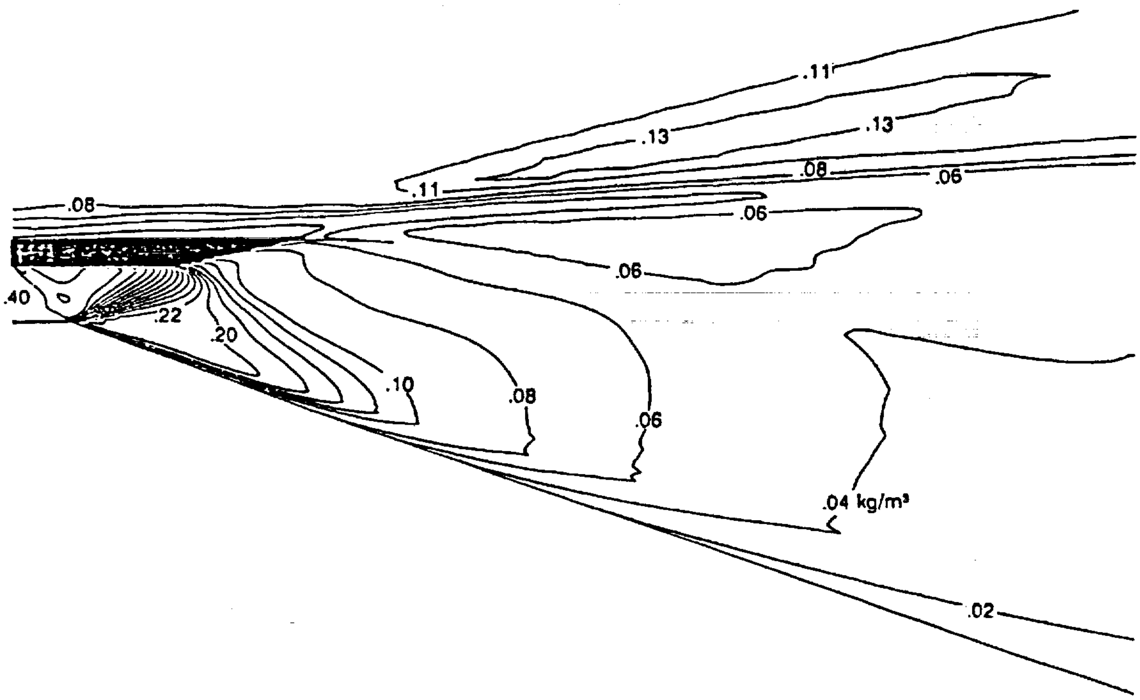

DENSITY CONTOURS MAX: .450 MIN: .0068 DELTA: .023 kg/m³

Figure 5.11 Case 2 density contours (fixed grid)

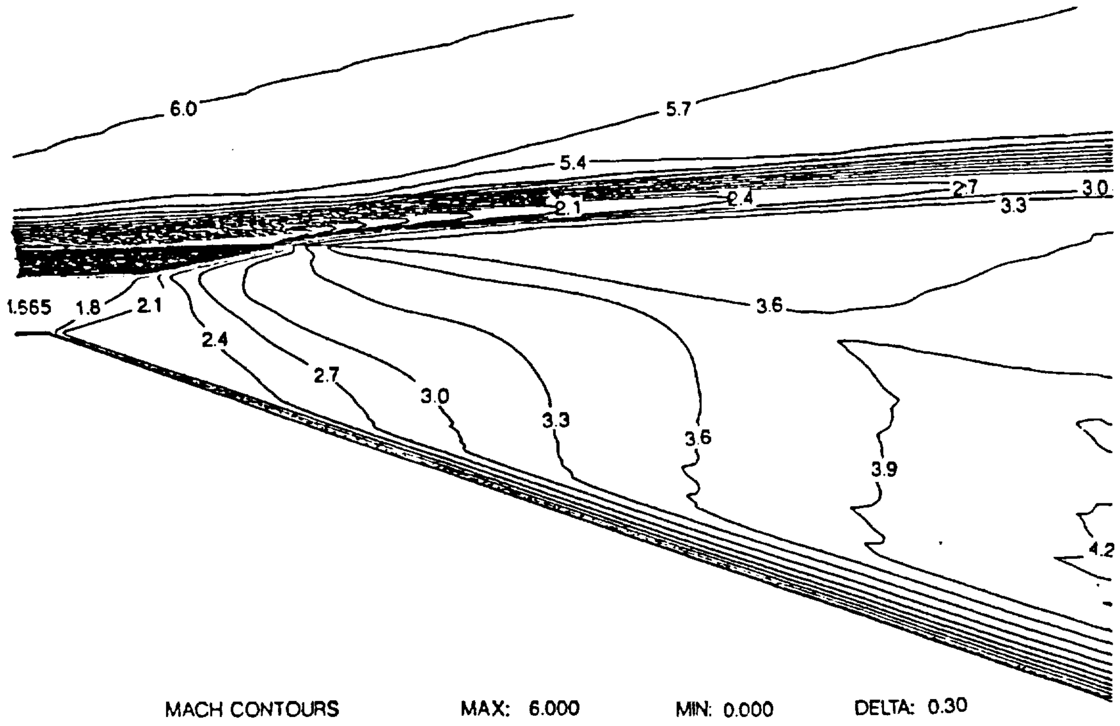

Figure 5.12 Case 2 Mach contours (fixed grid)

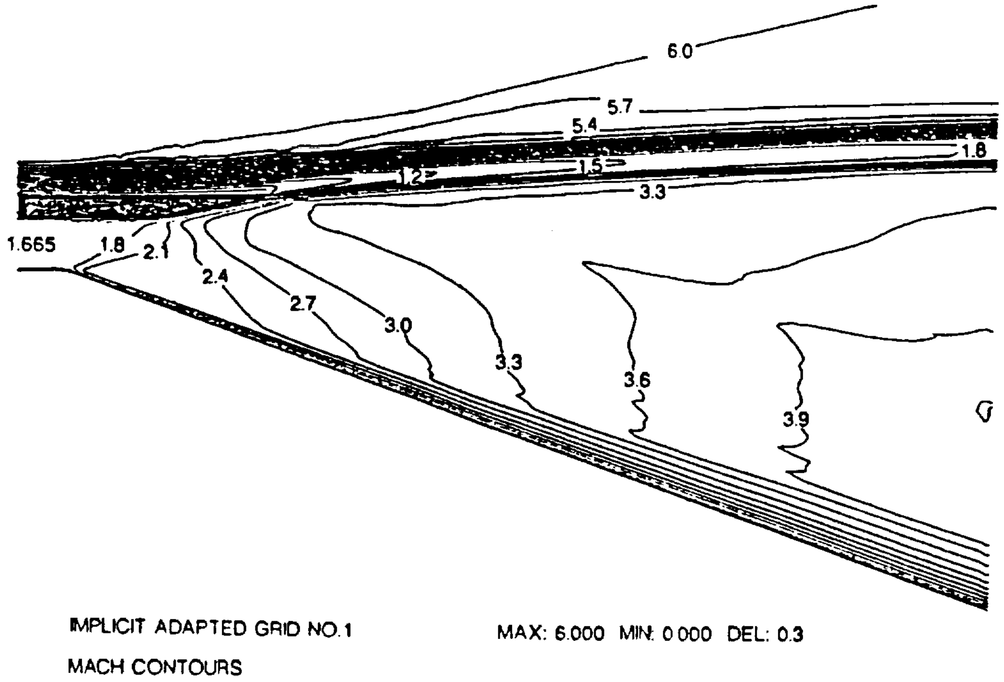

Figure 5.13 Case 2 Mach contours (adapted grid)

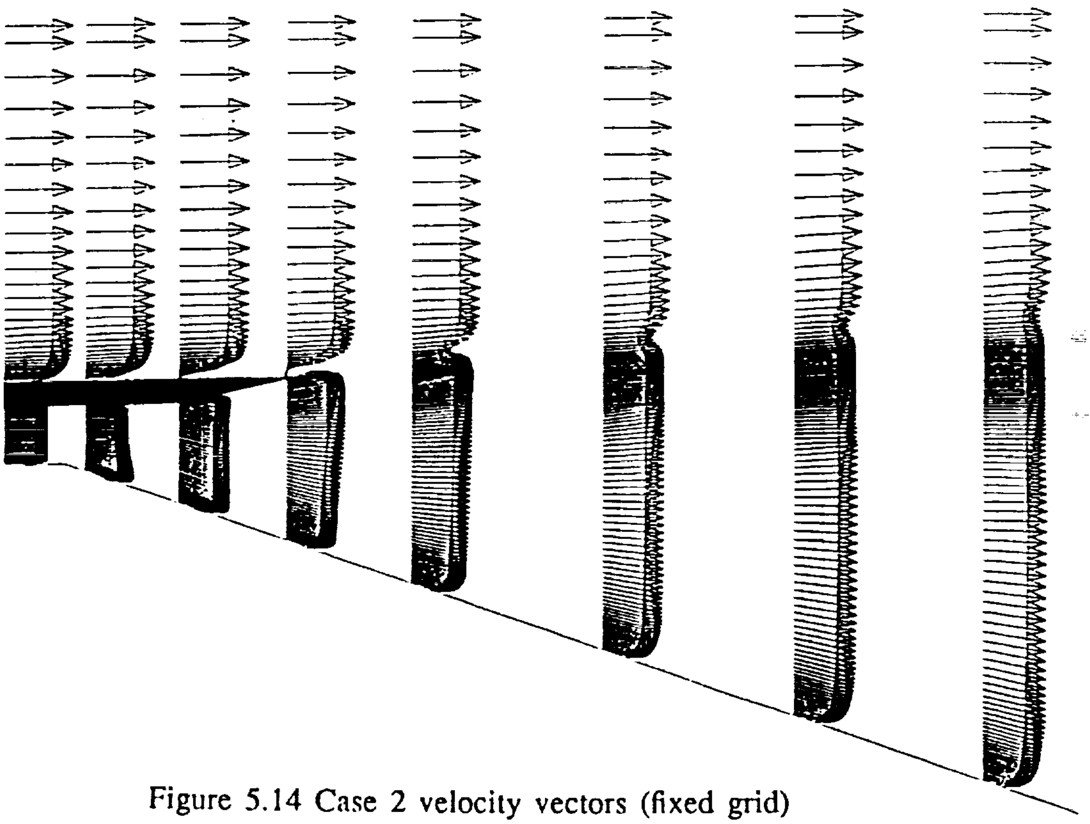

Figure 5.14 Case 2 velocity vectors (fixed grid)

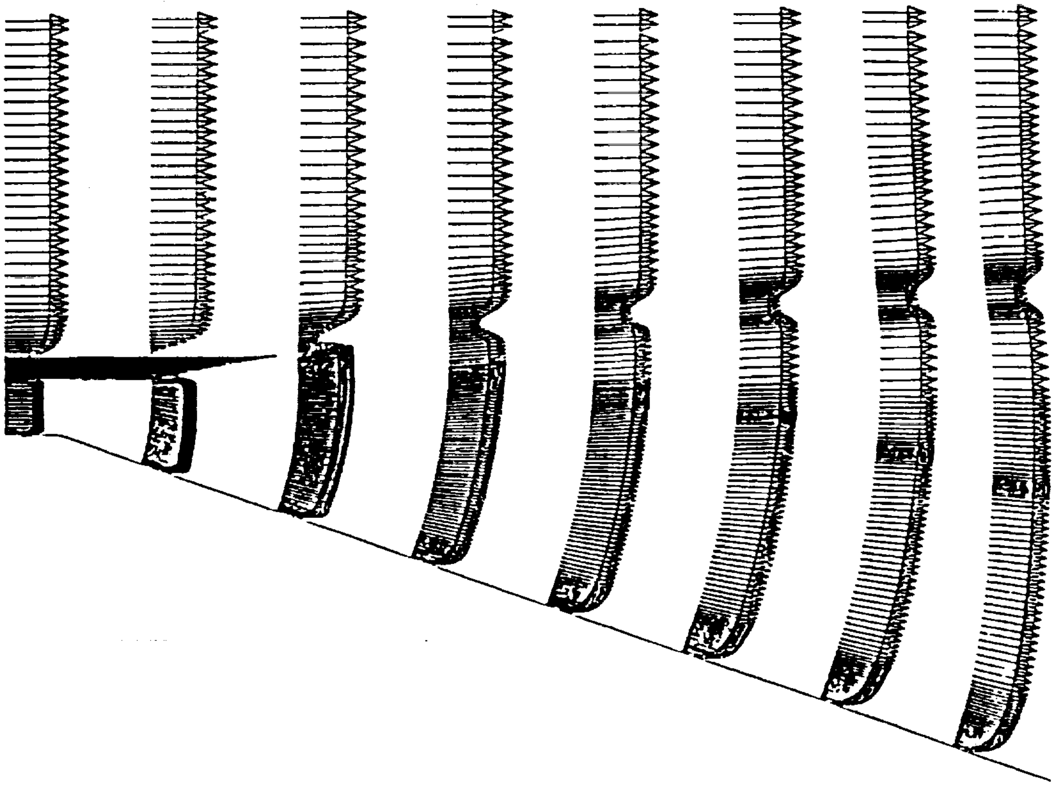

Figure 5.15 Case 2 velocity vectors (adapted grid)

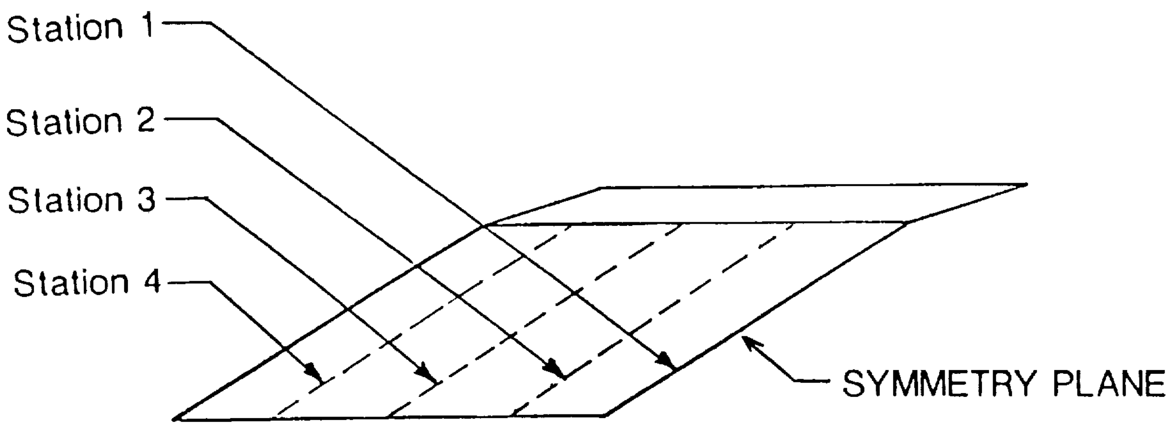

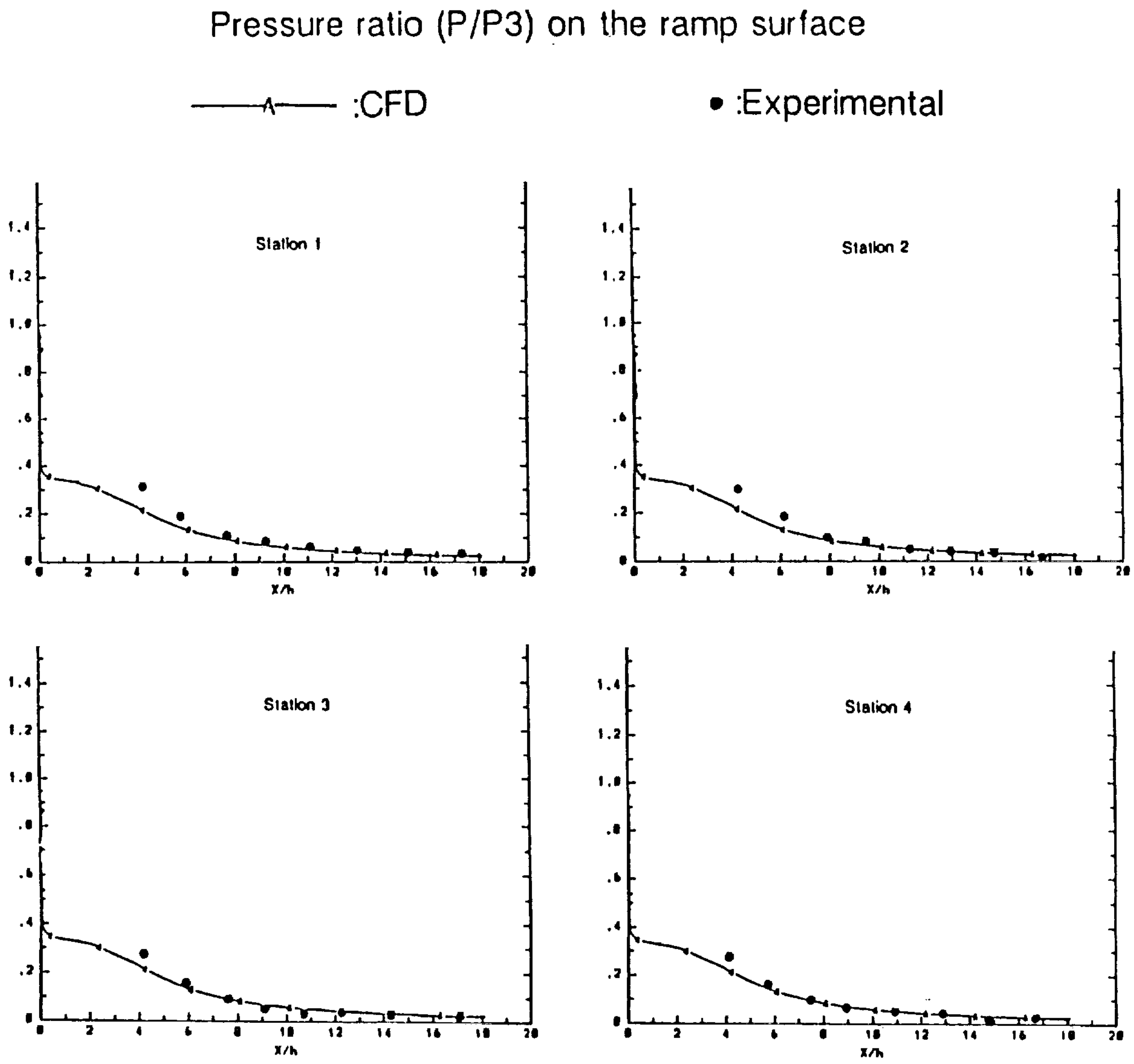

Figure 5.16 Case 3 spanwise surface pressure contours

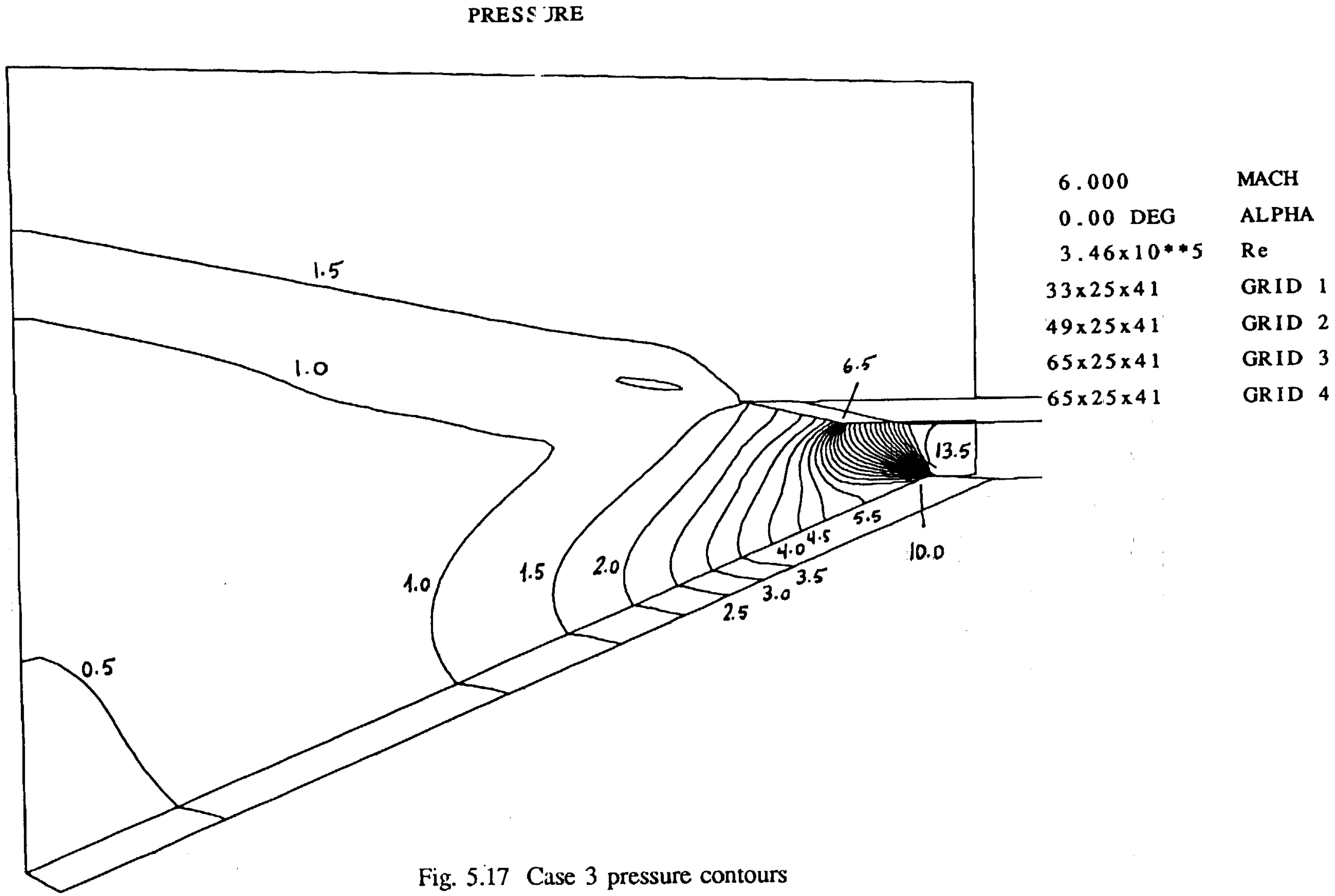

Fig. 5.17 Case 3 pressure contours

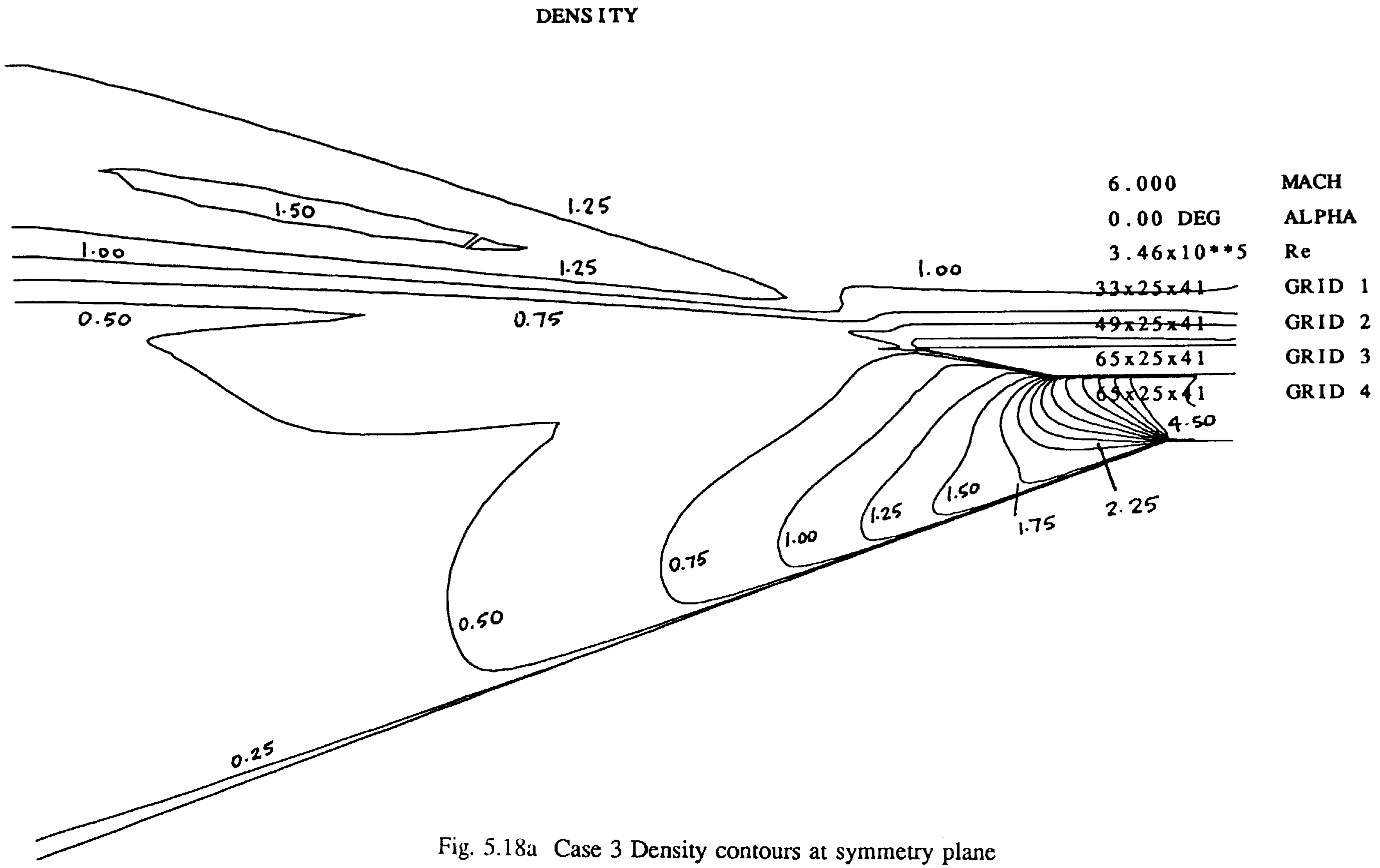

Fig. 5.18a Case 3 Density contours at symmetry plane

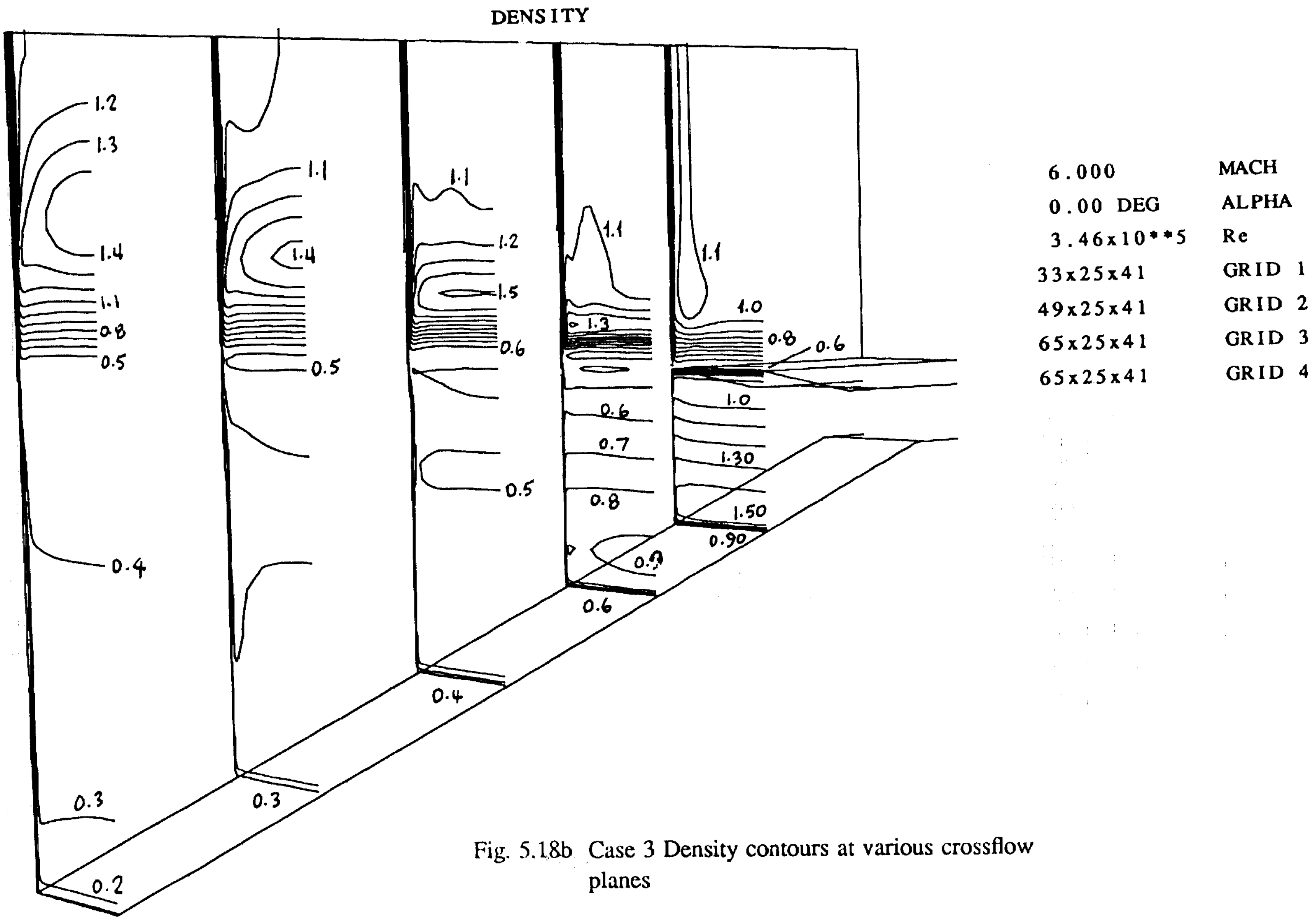

Fig. 5.18b Case 3 Density contours at various crossflow planes

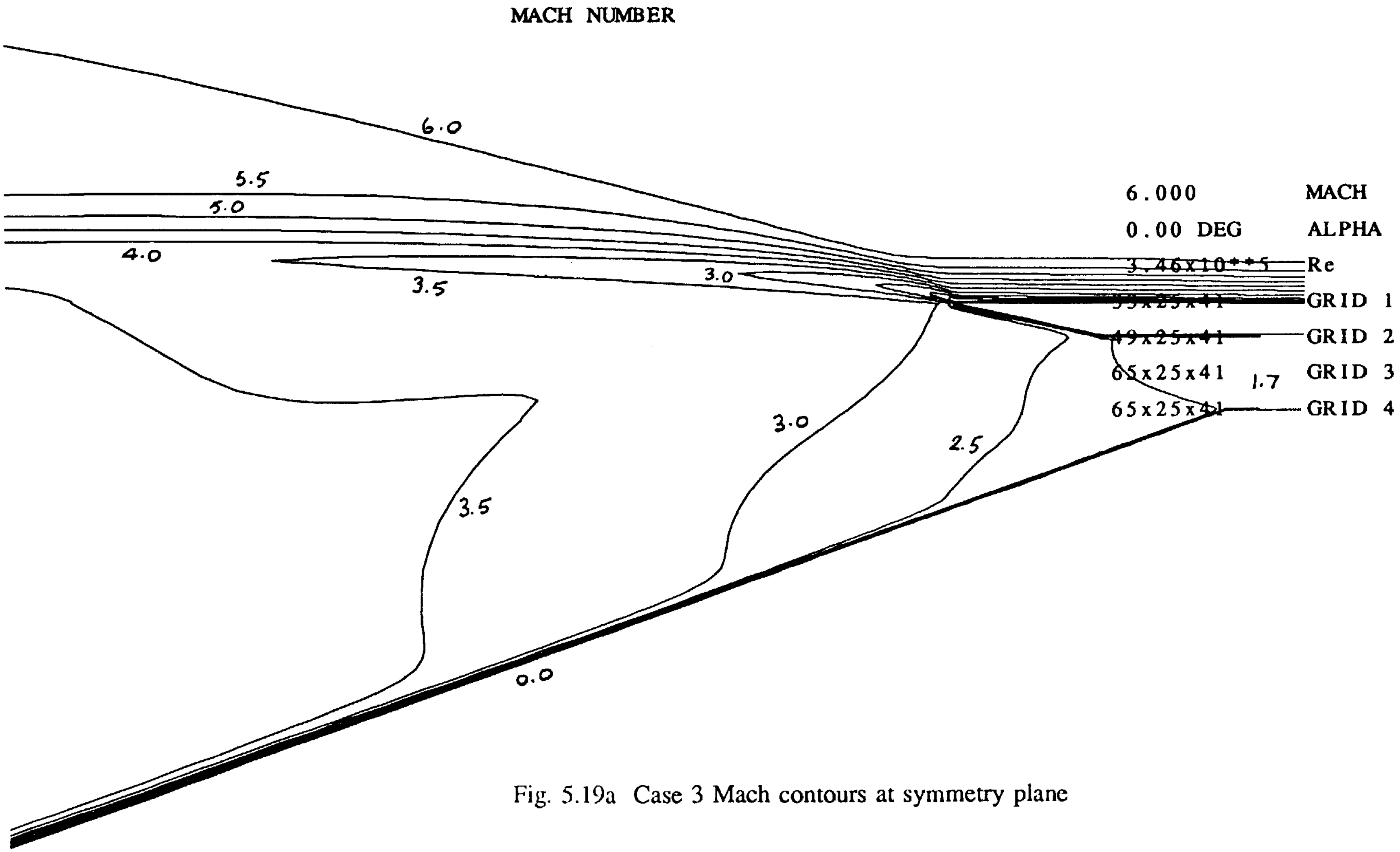

Fig. 5.19a Case 3 Mach contours at symmetry plane

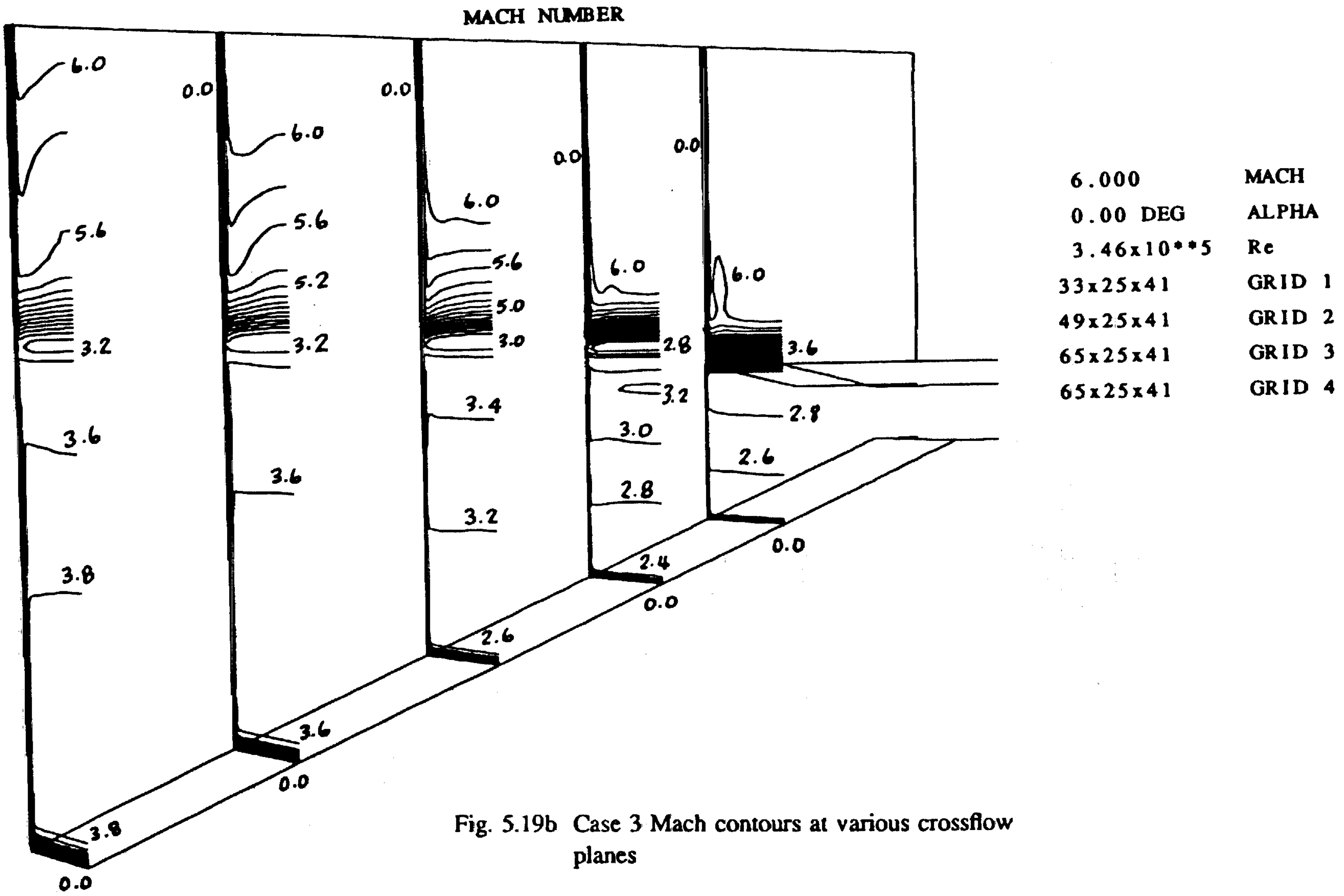

Fig. 5.19b Case 3 Mach contours at various crossflow planes

Appendix A

COLD GAS SIMULATION OF HOT EXHAUST PRODUCTS

In order to accurately simulate the nozzle exhaust flow from scramjet engine modules using scaled test models, several nondimensional parameters must be matched between the test flow and the exhaust products of the actual scramjet engine. For inviscid flow similitude, the parameters which must be matched include the geometry scales between the actual nozzle afterbody and the model, the ratio of static pressures (internal to external), the Mach numbers, and the flow directions at geometrically similar locations within the flow fields. If these parameters are all matched at the nozzle exit plane, the wave systems and Mach lines which emanate from the test model nozzle will match those of the actual engine.

If a simulant gas is used, in lieu of the hot scramjet exhaust products (which are very difficult to use in a conventional wind tunnel), the ratio of specific heats (γ) must also be matched [1] so that the wave systems will travel at the same speed. This is due to the fact that the speed of sound in a gas is directly related to γ by the relationship $a=\gamma RT$. If the pressure distribution on the afterbody surface of the model is to match that of the actual nozzle-afterbody, the system of expansion and compression waves must be similar.

The use of simulant gases can be used to simulate the flow of hot scramjet exhaust products at greatly reduced temperature levels, and allow for the scaled scramjet nozzle-afterbody model testing in a conventional wind tunnel.

Several different gases have been identified for use as a scramjet exhaust simulant gas [1], some of which are simple mixtures of Freon and Argon. In Fig. A.1 the variation of γ with temperature is shown for a 70% $F_{13}B_1$ (Freon-13) + 30% Argon mixture (by volume), along with the γ variation of a scramjet exhaust gas. As seen in this figure, the γ values of the Freon-Argon mixture match those of the exhaust gas at a significantly lower temperature.

When air is used as the simulant gas, some error is introduced into the experimental pressures due to the difference in specific heat ratios. The gamma value for air is approximately constant at 1.4 over the temperature which is suitable for conventional wind tunnel testing. However, air is much less costly to use in a wind tunnel test, so it remains a good candidate for preliminary analysis.

The requirements for viscous similitude are somewhat more restrictive than those of the inviscid flow. In addition to the aforementioned parameters, the Reynolds number, Prandtl number, and Schmidt number must also be matched. In this study however, the effects of surface heat transfer and the diffusion of the exhaust gases into the freestream are not considered, so it is not necessary to match the Prandtl and Schmidt numbers, and only the Reynolds number becomes important.

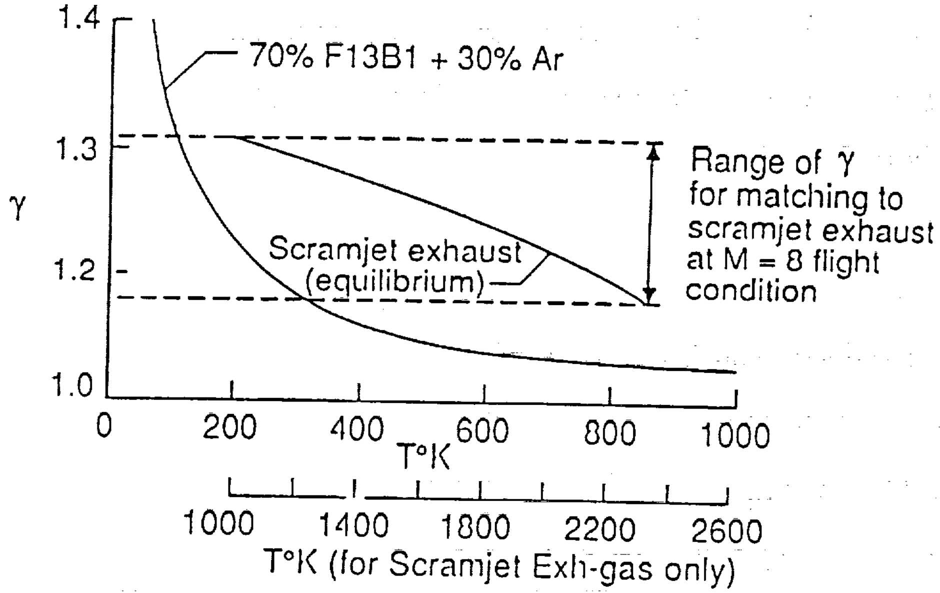

Figure A.1 Matching of specific-heat-ratios between simulant gas and exhaust prod- ucts

Appendix B

ADAPTIVE GRIDS

The adaptive grid methodology used in this study is based on the work of Nakahshi and Deiwert [31,32]. In this method, the solution adaptive grids are generated based on a tension and torsion spring analogy. The tension spring connects adjacent grid points to each other and controls the grid spacing so that the grid density is highest in regions where strong gradients exist, such as shocks and shear layers. Torsion springs, which are located at each grid node, are used to prohibit the grid from becoming excessively skewed.

B.1 One-dimensional Grid Adaption

Consider a one-dimensional flow in the η–direction, for which the flows domain has been discretized into a grid with constant spacing. Let point A on this grid (Fig. B.1) be connected to points B and C by tension springs whose constants are $k_{i,\,j\text{-}1}$ and $k_{i,\,j}$ respectively.The grid points are redistributed along the η–constant lines by computing the spring constant based on the gradient of a given flow parameter, f_i, as:

$$k_{i,j} = 1 + \frac{C_1 |f_{i,j+1} - f_{i,j}|}{(s_{i,j+1} - s_{i,j})} \tag{B.1}$$

where C_1 is a constant, and $s_{i,j}$ is the arc length calculated from point (i,1) along a η_i coordinate line. The new location of grid point $s_{i,j}$ is computed using the relationship of Eq. (B.1) as:

$$k_{i,j}(s_{i,j+1} - s_{i,j}) - k_{i,j-1}(s_{i,j} - s_{i,j-1}) = 0 \tag{B.2}$$

If the flow is strickly one-dimensional, the use of tension springs will allow for sufficient control over the adaptive grid; however, if the flow is two-dimensional and complex, the grid can become excessively skewed (an undesirable effect for most finite volume/difference solvers). To alleviate this problem, torsion springs are added to each grid node. The torsion springs control the inclination of line DA to that of a reference line. If the torsion spring constant is denoted by H (Fig. B.2), the force at point A is computed as:

$$F_{torsion} = -H_{i-1,j}(\theta_{DA} - \phi) \tag{B.3}$$

where θ_{DA} is an inclination of line DA and ϕ is the inclination of the reference line. The reference line is chosen as an extension of FD to avoid kinks in the ξ–line at point D. A balance equation for the complete spring system is given as:

$$k_{i,j}(s_{i,j+1} - s_{i,j}) - k_{i,j-1}(s_{i,j} - s_{i,j-1}) - H_{i-1,j}(\theta_{i-1,j} - \phi_{i-1.j}) = 0 \tag{B.4}$$

If θ and ϕ are written in terms of the arc length $s_{i,j}$, of the intersection of the reference line DA' and the η_i coordinate (Fig. B.2) Eq. (B.4) can be rewritten as:

$$k_{i,j-1}s_{i,j-1} - (k_{i,j} + k_{i,j-1} + H_{i-1,j})s_{i,j} + k_{i,j}s_{i,j+1} = -H_{i-1,j}\bar{s}_{i,j} \tag{B.5}$$

This results in a tridiagonal system of equations for $s_{i,j}$ which is easily solved. In this analysis, only the torsion force on the upstream side (η_{i-1}) influences the distribution at η_i. This allows for the use of a simple marching type algorithm to be used in the solution of $s_{i,j}$.

B.2 Extension of Grid Adaption to Multi-dimensions

The basic algorithm described above can be extended to two-direction adaption by performing multiple sweeps. In each sweep, the adaption is applied in a single direction only. This is analogous to the alternating direction implicit (ADI) logic used in the flow solver described in chapter three. This concept is easily shown in Fig. B.3. The two-dimensional adapted grid is constructed from two single dimensional adapted grids. Once the grid is "adapted" to the flowfield gradients, the solution field is interpolated onto the new grid using second-order, one dimensional Lagrange interpolations.

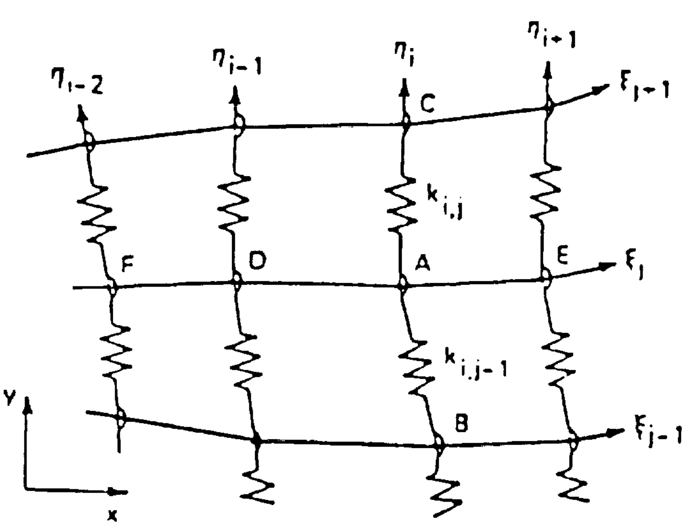

Figure B.1 Tension spring analogy for the one-dimensional adaptive grid

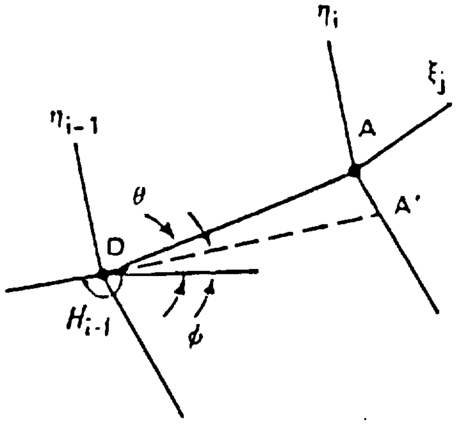

Figure B.2 Torsion spring analogy for the adaptive grid

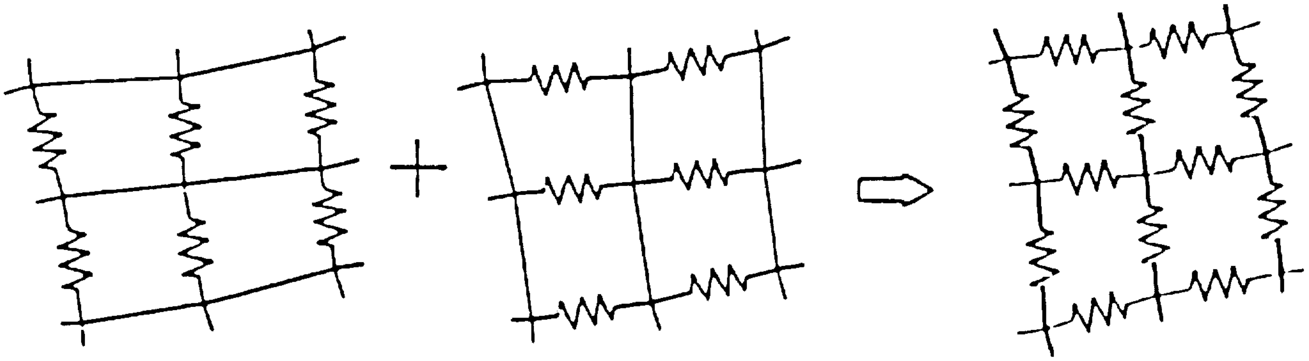

Figure B.3 Construction of a two-dimensional adapted grid using one- dimensional sweeps

NASA
National Aeronautics and
Space Administration

Report Documentation Page

1. Report No. NASA CR-4406	2. Government Accession No.	3. Recipient's Catalog No.

4. Title and Subtitle Viscous Computations of Cold Air/Air Flow Around Scramjet Nozzle Afterbody	5. Report Date October 1991
	6. Performing Organization Code
7. Author(s) Oktay Baysal and Walter C. Engelund	8. Performing Organization Report No.
	10. Work Unit No. 505-59-30-01
9. Performing Organization Name and Address Old Dominion University Mechanical Engineering & Mechanics Department Norfolk, Virginia 23529	11. Contract or Grant No. NAG1-811
12. Sponsoring Agency Name and Address National Aeronautics and Space Administration Langley Research Center Hampton, Virginia 23665-5225	13. Type of Report and Period Covered Contractor Report
	14. Sponsoring Agency Code

15. Supplementary Notes

Langley Technical Monitor: David S. Miller

16. Abstract

The flow field in and around the nozzle-afterbody section of a hypersonic vehicle was computationally simulated. The compressible, Reynolds averaged, Navier-Stokes equations were solved by an implicit, finite-volume, characteristic-based method. The computational grids were adapted to the flow as the solutions were developing in order to improve the accuracy. The exhaust gases were assumed to be cold. The computational results were obtained for the two-dimensional longitudinal plane located at the half-span of the internal portion of the nozzle for over-expanded and under-expanded conditions. Another set of results were obtained, where the three-dimensional simulations were performed for a half-span nozzle. The surface pressures were successfully compared with the data obtained from the wind tunnel tests. The results help in understanding this complex flow field, and in turn should help the design of the nozzle-afterbody section.

17. Key Words (Suggested by Author(s)) scramjet nozzle-afterbody flows, supersonic-hypersonic mixing flows, computational fluid dynamics, and hypersonic plane	18. Distribution Statement Unclassified-Unlimited Subject Category 02

19. Security Classif. (of this report) Unclassified	20. Security Classif. (of this page) Unclassified	21. No. of pages 76	22. Price A05

NASA FORM 1626 OCT 86

For sale by the National Technical Information Service, Springfield, Virginia 22161-2171

NASA-Langley, 1991